Mon. Not. R. Astron. Soc. **000**, 1–23 (2006) Printed 4 February 2009 (MN LATEX style file v2.2)

A new search for distant radio galaxies in the Southern hemisphere – III. Optical spectroscopy and analysis of the MRCR–SUMSS sample⋆

J. J. Bryant[1]†, H. M. Johnston[1], J. W. Broderick[1], R. W. Hunstead[1], C. De Breuck[2], and B. M. Gaensler[1,3]
[1] *SIfA, School of Physics A29, The University of Sydney, NSW 2006, Australia*
[2] *European Southern Observatory, Karl Schwarzschild Straße 2, D-85748 Garching, Germany*
[3] *Harvard-Smithsonian Center for Astrophysics, 60 Garden Street, Cambridge MA 02138, USA*

ABSTRACT

We have compiled a sample of 234 ultra-steep-spectrum(USS)-selected radio sources in order to find high-redshift radio galaxies (HzRGs). The sample is in the southern sky at $-40^\circ < \delta < -30^\circ$ which is the overlap region of the 408-MHz Revised Molonglo Reference Catalogue, 843-MHz Sydney University Molonglo Sky Survey (the MRCR–SUMSS sample) and the 1400-MHz NRAO VLA Sky Survey. This is the third in a series of papers on the MRCR–SUMSS sample. Here we present optical spectra from the ANU 2.3-m telescope, ESO New Technology Telescope and ESO Very Large Telescope for 52 of the identifications from Paper II, yielding redshifts for 36 galaxies, 13 of which have $z > 2$. We analyse the K–z distribution and compare 4-arcsec-aperture magnitudes with 64-kpc aperture magnitudes in several surveys from the literature; the MRCR–SUMSS sample is found to be consistent with models for 10^{11}–$10^{12}\,\mathrm{M}_\odot$ galaxies. Dispersions about the fits in the K–z plot support passive evolution of radio galaxy hosts since $z > 3$. By comparing USS-selected samples in the literature, we find that the resultant median redshift of the samples shown is not dependent on the flux density distribution or selection frequency of each sample. In addition, our finding that the majority of the radio spectral energy distributions remain straight over a wide frequency range suggests that a k-correction is not responsible for the success of USS-selection in identifying high redshift radio galaxies and therefore the steep radio spectra may be intrinsic to the source or a product of the environment. Two galaxies have been found to have both compact radio structures and strong self-absorption in the Lyα line, suggesting they are surrounded by a dense medium. For the bulk of the sources, spectral line ratios show that photoionisation is the primary excitation process.

Key words: galaxies: active – surveys – galaxies: high-redshift – infrared: galaxies – radio continuum: galaxies.

1 INTRODUCTION

Hierarchical models of galaxy formation predict that massive galaxies formed through many mergers of smaller systems, with continuous bursts of star formation. However, there is solid evidence that the most massive galaxies in the local Universe formed their stars very early in the history of the Universe (Stanford, Eisenhardt & Dickinson 1998; Nelson et al. 2001; Thomas et al. 2005). In order to fit current galaxy-formation models, feedback processes have been introduced in which the energy input from a central massive black hole quenches the star formation by heating the interstellar gas (Springel et al. 2005; De Lucia et al. 2005; Bower et al. 2006). Such modifications appear to overcome many of the shortcomings of previous hierarchical models, but although the quenching of star formation is attributed to the onset of a galactic wind driven by ionising radiation and/or

⋆ Based on observations obtained at the ESO Very Large Telescope (VLT) and New Technology Telescope (NTT) as part of program numbers 077.A-0471 and 079.A-0504 and the ANU 2.3 m telescope.

† E-mail: jbryant@physics.usyd.edu.au

mechanical energy from the radio jets, the physical mechanisms for this are poorly understood. In contrast, there is observational evidence to suggest that the radio jets associated with some supermassive black holes might *trigger*, rather than suppress, star formation in high-redshift galaxies (Rees 1989; Bicknell et al. 2000; Klamer et al. 2004; Croft et al. 2006). There are also plausible arguments to suggest that both processes operate, with radio jets first triggering star formation and then later driving a galactic wind (Silk 2005). The interplay between mergers and feedback associated with active galactic nuclei (AGN) is likely to affect the evolution of all massive galaxies, not just the extreme bright end of the luminosity function (Croton et al. 2006). However, it is the most massive galaxies at high redshift that provide the most stringent constraints on these processes.

The star formation rate density in the early Universe is dominated by the most massive galaxies in the sample volume (see fig. 2 of Feulner et al. 2005). In Rocca-Volmerange et al. (2004, fig. 5), radio galaxies have been identified to be more massive than optically-selected galaxies at each redshift, with stellar masses of $\sim 10^{12}\,\mathrm{M}_{\odot}$, which is $5-10$ times more massive than the largest galaxies in most optical surveys. The star formation rate density of the Universe has been shown to peak at $2 < z < 3.5$ (Lilly et al. 1996; Madau et al. 1996; Hopkins 2004; Hopkins & Beacom 2006, fig. 2) and since radio galaxies are the most massive and dominate the star formation rate at these epochs, they are crucial to understanding early galaxy evolution.

We have conducted a survey of ultra-steep-spectrum (USS) radio sources in the Southern Hemisphere, designed to find high-redshift ($z > 2$) radio galaxies so as to carry out a detailed quantitative study of their environments. This is the first USS survey in the South to use large, deep low-frequency catalogues to mine a large area of sky, and it became possible with the completion of the Sydney University Molonglo Sky Survey at 843 MHz (SUMSS; Bock et al. 1999; Mauch et al. 2003) and the reanalysis of the 408-MHz Molonglo Cross survey (Large et al. 1981) to give the more sensitive revised Molonglo Reference Catalogue (MRCR; Crawford, private communication).

The details of the sample selection, and the 1384- and 2368-MHz radio imaging of the MRCR–SUMSS sample were presented in Broderick et al. (2007, hereafter Paper I). The K-band imaging and identification of the counterparts to 175 of the radio sources were presented in Bryant et al. (2009, hereafter Paper II). The current paper includes the followup spectroscopy for the sources in Paper II and a complete discussion of the sample using the radio, K-band, redshift and spectral line information. A following paper will discuss the environments of the $z > 2$ galaxies and what that can tell us about the early evolution of massive galaxies.

We have adopted a flat, Λ cold dark matter cosmology with $H_0 = 71$ km s^{-1} Mpc^{-1}, $\Omega_{\mathrm{M}} = 0.27$ and $\Omega_{\Lambda} = 0.73$.

2 OBSERVATIONS AND DATA REDUCTION

2.1 Target selection and radio and K-band imaging

The target selection, radio observations and K-band imaging were discussed extensively in Papers I and II. A very brief summary is given here.

The MRCR–SUMSS sample was formed by cross-matching the revised 408-MHz Molonglo Reference Catalogue (MRCR), the 843-MHz SUMSS catalogue and the 1400-MHz NVSS catalogue (Condon et al. 1998) in the region where all three catalogues overlap (declination $-30°$ to $-40°$). We then selected sources with a spectral index[1] between 408 and 843 MHz, $\alpha_{408}^{843} \leqslant -1.0$ and Galactic latitude $|b| > 10°$. We further eliminated any sources that had another NVSS source within 100 arcsec to minimize the effects of source confusion.

Follow-up radio images were obtained with the Australia Telescope Compact Array (ATCA) at 1384 and 2368 MHz for the full sample, to pinpoint the K-band identification and investigate the radio structure. These are detailed in Paper I. Twenty-nine of the MRCR–SUMSS sources were also observed at 4800 and 8640 MHz; those data are presented in Paper II.

K-band (2.2μm) observations were made with the 3.9-m Anglo-Australian Telescope's (AAT) IRIS2 detector (Gillingham & Jones 2000) and with PANIC (Martini et al. 2004) on the 6.5-m Magellan Baade telescope at Las Campanas Observatory. Full details of the K-band imaging and reduction are given in Paper II.

2.2 Spectroscopy

Spectra for our sources were obtained using three spectrograph/telescope combinations. Sources with optical identifications from the SuperCOSMOS Sky Survey (Hambly et al. 2001) were observed using the 2.3-m telescope of the Australian National University (ANU) at Siding Spring Observatory, NSW. Identifications with $K \lesssim 19$ were observed with the 3.6 m ESO New Technology Telescope (NTT), and the faintest targets ($K > 19$) were observed using the 8 m ESO Very Large Telescope (VLT). For both the NTT and VLT observations, to acquire the faint targets into the slit, we used blind offsets from a nearby ($\lesssim$1 arcmin) star in the K-band images. After a first exposure, we performed a quick data reduction. If the redshift was obvious, the next exposure was aborted to save observing time. The individual exposures were offset by 10 arcsec along the slit to allow subtraction of the fringing in the detector at red wavelengths.

The journal of observations is given in Table 1.

2.2.1 ANU 2.3m

We used the Dual-Beam Spectrograph (DBS; Rodgers, Conroy & Bloxham 1988) on the ANU's 2.3-m telescope on 2007 April 10–14. A plane mirror was used to direct all the light into the blue arm of the spectrograph in order to obtain complete wavelength coverage over the range 3500–11000 Å.

[1] Radio spectral index α is related to S_{ν}, the flux density at frequency ν, by $S_{\nu} \propto \nu^{\alpha}$

Table 1. Log of observations.

Date	Telescope	Instrument	Seeing (arcsec)
2006 June 22–23	VLT	FORS2	0.5–1.3
2006 July 27	NTT	EMMI	1.0–1.4
2007 April 10–14	ANU 2.3 m	DBS	1.5–3.0
2007 July 10–12	NTT	EMMI	0.6–1.0

The CCD is an E2V 2148×562 pixel detector with a spatial scale of 0.91 arcsec pixel^{-1}. We used the 158R grating, providing a dispersion of 4 Å pixel^{-1} and a spectral resolution of 8.9 Å. Severe fringing at the red end restricted the usable wavelength range to 3500–8000 Å; second order contamination was minimal. Conditions were variable, but mostly non-photometric, with poor seeing.

2.2.2 ESO/NTT

We used the ESO Multi-Mode Instrument (EMMI; Dekker, Delabre & D'Odorico 1986) on the NTT on 2006 July 25–27 and 2007 July 10–12. The conditions in 2006 were poor with the first two nights lost to weather; the third was non-photometric with 1.0–1.4-arcsec seeing. In 2007 the conditions were better, with seeing between 0.6 and 1.0-arcsec FWHM. We used grism #2 and a 1.5- or 1-arcsec slit; the latter was used in the better seeing conditions. The wavelength coverage was 3700–9700 Å, with a dispersion of 3.5 Å pixel^{-1}, a spectral resolution of 10.4 Å FWHM and the pixel size was 0.33 arcsec. To minimise the effects of differential atmospheric refraction, we observed the targets with the slit oriented at the parallactic position angle.

2.2.3 ESO/VLT

We used the FOcal Reducer and Spectrograph (FORS; Appenzeller et al. 1998) in visitor mode on the VLT on 2006 June 22–23. We used FORS2 on UT1 (Antu) with the 150I grism and 1-arcsec slit, providing a dispersion of 6.7 Å pixel^{-1} and a spectral resolution of 21.4 Å. The wavelength coverage was 3600–8500 Å. As the FORS instruments have a linear atmospheric dispersion corrector, we did not observe at the parallactic angle, and instead the slit position angle was chosen to avoid bright stars.

2.2.4 Data reduction

Data reduction was performed with the IRAF software suite, using standard procedures. We removed the bias and pixel-to-pixel gain variations from each frame, and then removed the cosmic rays using the IRAF task SZAP. We extracted spectra using the IRAF task APALL, extracting only the central few rows ($\sim$ 1 arcsec) to maximise the signal-to-noise ratio of the spectrum. This optimises our chance of finding a redshift, at the cost of not including all the flux from the object, particularly from any extended line emission. The same extraction aperture was used to extract a calibration spectrum from the arc lamp, which was then used to calibrate the one-dimensional spectrum in wavelength.

The spectra were flux-calibrated by comparing with the spectrum of a spectrophotometric standard taken on the same night. No correction was made for Galactic reddening.

3 RESULTS

Table 2 lists all the MRCR–SUMSS sources for which we have taken spectra. The K-band images with radio contours for these objects were presented in Paper II. Some sources met our selection criteria, but were also part of the SUMSS–NVSS sample (De Breuck et al. 2004, Paper I), and were therefore not reobserved. For those sources, the K-band magnitudes and positions given are from De Breuck et al. (2004).

The columns in Table 2 are:
(1) NVSS source name.
(2) K-band magnitude in a 4-arcsec-diameter aperture. Some sources are obscured by foreground stars (see column 6) which contaminate the listed magnitude. Sources marked SC were visible on the SuperCOSMOS UKR fields and no K-band image was obtained (see Paper II). Our analysis exclusively used magnitudes in a 4-arcsec aperture, and the justification for this choice is given in Paper II.
(3) K-band magnitudes in equivalent 64-kpc apertures, which were calculated from 8-arcsec-aperture magnitudes, following the method of Eales et al. (1997). Only radio galaxies (not QSOs) which have redshifts and 8-arcsec-aperture magnitudes in Paper II have been converted. The limitations on these 64-kpc-aperture magnitudes were discussed in Paper II and are discussed further in Section 4.1.2.
(4) & (5) RA and DEC (J2000) of the K-band identification. One source which had no K-band identification is marked "—". The sources which had SuperCOSMOS identifications have the SuperCOSMOS position listed.
(6) Spectroscopic redshift. The wavelength of each line was determined by fitting a Gaussian on top of a continuum. Occasionally spurious lines were introduced by the fringing in the CCD; we required that features be visible in both exposures to be counted as real. The redshift quoted is the average of the redshifts derived from individual lines; the error is the scatter in this average, with uncertainties due to the line fitting and wavelength calibration added in quadrature. The sources marked 'continuum' had continuum but no lines, while those marked 'undetected' showed no continuum or line emission. Some objects are obscured by a foreground star and are listed as 'obscured'. Objects with emission lines broader than $> 3000\,\mathrm{km\,s^{-1}}$ have been classified as QSOs [2] and are marked with a 'Q'.
(7) Origin of the spectra. On the NTT, EMMI was the spectrograph, while FORS2 was the instrument on the VLT. 'DB' refers to objects from De Breuck et al. (2004, 2006).
(8) Linear size in kpc using the largest angular size measurements at 2368 MHz unless marked with a footnote.
(9) Rest-frame luminosity at 1.4 GHz in W Hz^{-1}. Luminosities were calculated using the 5-point spectral index from Paper II (table 2) unless marked by a footnote.

[2] NVSS J144932−385657 has one line with FWHM$>$ $3000\,\mathrm{km\,s^{-1}}$ but it is faint and the error on the width is large; since the other lines are narrow we do not classify it as a QSO.

Of the 164 sources with K-band or SuperCOSMOS counterparts in Paper II, spectra were obtained for 52 objects listed in Table 2, including 46 new spectra and six that are common to the SUMSS–NVSS sample and therefore have spectra in De Breuck et al. (2006). NVSS J231727−352606 is in both the SUMSS–NVSS and MRCR–SUMSS samples, and has a K-band magnitude limit listed in De Breuck et al. (2004) and a redshift from De Breuck et al. (2006); our new, deeper limiting magnitude (see Paper II) is shown in the table. NVSS J103441−394957 and the combined source NVSS J023601−314204/J023605−314235 have very faint red identifications in SuperCOSMOS, and were retained in the sample because the identification was not located until we had high-resolution ATCA images.

The spectroscopy has resulted in 36 confirmed redshifts, 12 continuum spectra, one that remained undetected and three that are obscured by stars. The spectra are shown in Fig. 1; they were smoothed lightly for the plots, using (typically) a 3-pixel boxcar.

Parameters of the emission lines were measured following procedures similar to those described in Röttgering et al. (1997); these parameters are listed in Table 3. The line centre and width (FWHM) were determined by fitting a Gaussian on top of a continuum; the line flux was obtained by direct summation of the flux above the continuum over a wavelength range four times the FWHM, except where such a width would also include neighbouring lines. No attempt has been made to de-blend lines. The location of the continuum was determined by eye separately for each line. This is the major source of error in the line ratios. The errors on the line fluxes and widths were estimated by comparing the measured values using different continuum levels; for some of the weaker lines, these errors are substantial. Because we extracted the spectra from only the central few rows of each object (see Section 2.2.4) we have not in general included all the flux from each emission line, so the line ratios we derive are characteristic of the nuclear regions only.

Thirty-three per cent of the redshifts obtained are in the range $2 < z < 3.5$, corresponding to the epoch in which the star formation rate density of the Universe was at a maximum (see Section 1). These objects will form part of our sample for follow-up observations to look at the clustering properties and environments of massive galaxies at that epoch.

Three of the possible identifications turned out to be M-stars. These are assumed to be misidentifications with foreground stars rather than radio stars, as the surface density of radio stars from Helfand et al. (1999) is much lower than our observed surface density of M-star radio identifications. The fraction of contaminating stars is similar to the SUMSS–NVSS sample in which three out of 35 spectra were misidentified stars. The stars are not included in our analysis. Twelve sources (23 per cent) showed a continuous spectrum with no emission lines and one was not detected, leaving 25 per cent of the galaxy spectra with undetermined redshifts. This is a smaller fraction than in the SUMSS–NVSS sample and the USS sample of De Breuck et al. (2001) which found 28 per cent and 35 per cent respectively. Of our twelve continuum sources, one was a spectrum taken with the ANU 2.3-m in which the S/N was insufficient to detect any lines and will be reobserved on a larger telescope. Six were NTT spectra which may need to be repeated on the VLT to improve the signal-to-noise ratio, and the remaining five were VLT spectra. The 'redshift desert' is the region $1 < z < 2.3$ where the strong [O II]λ3727 line has been shifted out of the spectral window, but Lyα has not yet moved into the window. The continuum sources may be in this redshift range or, alternatively, the Lyα line may be self-absorbed and the other emission lines too weak to be detected.

3.1 Notes on individual sources

NVSS J023601−314204/J023605−314235 (combined source, see Paper II): The spectrum shows no emission lines, but the redshift is secure based on stellar features.
NVSS J103441−394957: The spectrum shows broad QSO emission lines and the radio source has a large linear size.
NVSS J103615−321659: We proposed in Paper II that this may be a double source with very unequal lobes. While our higher resolution images did not show a double structure as the fainter lobe was resolved out, our spectrum is that of a $z = 2.136$ galaxy. This high redshift supports our identification as it would be very unlikely for a $z > 2$ galaxy to coincidentally be as close as this to a USS radio source.
NVSS J105917−303658: The emission lines are broad, typical of a quasar and it has compact radio structure with a largest angular size of 1.0 arcsec. The C IVλ1549 line shows strong self-absorption and the blue wing of the Lyα line appears to have been absorbed completely (see Fig. 14). Absorption at the redshift of the host galaxy was found by Baker et al. (2002) in almost all compact steep-spectrum radio-loud quasars.
NVSS J112641−383950: The line at 7468Å; (marked with an asterisk in Fig. 1) is the λ1305 O I+Si II line appearing in second order.
NVSS J140223−363539: The 8640-MHz image in Paper II showed contours extending towards an object 2 arcsec south-west of the 2368-MHz peak. A spectrum of this object has confirmed the redshift to be 2.796. While it does not align with the radio structure, it would be highly unlikely that this could be a separate high-redshift object that coincidentally is near the radio source. The NVSS centroid is 2.5-arcsec north of the claimed identification. That may indicate the presence of another faint lobe to the north which is resolved out in the ATCA observations, suggesting that it could have a wide-angled tail structure. For the time being we assume the high-redshift source to be the identification due to its redshift, but we cannot explain the offset from the expected position.
NVSS J140854−382731: The redshift is based on a single line, which we identify as [O II]λ3727, and the marginal presence of other lines in the spectrum.
NVSS J141428−320637: Shows evidence of recent star formation, with Hδ absorption characteristic of an A-star population.
NVSS J144206−345115: A quasar, with broad lines and associated absorption (see Fig. 14).
NVSS J151020−352803: There is only one bright line in the spectrum, which is spatially extended over 3.6 arcsec, which we identify as Lyα, based on the marginal presence of confirming lines.
NVSS J151215−382220: No lines were identified, but the

Table 2. Spectroscopy results including redshifts and the derived linear sizes and rest-frame luminosities. Details of each column are given in Section 3.

(1) Name	(2) K ($4''$ ap.) (mag)	(3) K (64 kpc) (mag)	(4) RA_{J2000} K-band (h m s)	(5) DEC_{J2000} K-band ($^\circ$ $'$ $''$)	(6) Redshift	(7) Origin	(8) Radio linear size (kpc)	(9) $L_{1.4\,GHz}$ (W Hz^{-1})
NVSS J001506−330155	17.6 ± 0.2		00:15:06.31	−33:01:54.0	continuum	NTT		
NVSS J003445−372348	17.0 ± 0.1		00:34:45.66	−37:23:47.4	continuum	NTT		
NVSS J011606−331241[i]	18.6 ± 0.2	18.0	01:16:06.77	−33:12:42.8	0.352 ± 0.001	DB	31.5	9.9×10^{24}
NVSS J023601−314204[a]	SC		02:36:03.99	−31:42:22.2[b]	0.500 ± 0.001	NTT	357.7	5.1×10^{25}
NVSS J023605−314235[a]								
NVSS J101008−383629	18.9 ± 0.2		10:10:08.02	−38:36:29.2	continuum	VLT		
NVSS J103441−394957	SC		10:34:42.10	−39:49:58.2[b]	1.832 ± 0.008 **Q**	2.3 m	247.3	1.3×10^{27}
NVSS J103615−321659	19.3 ± 0.2		10:36:15.26	−32:16:57.4	2.136 ± 0.012	VLT	87.5	$3.0 \times 10^{27\,n}$
NVSS J105917−303658	18.8 ± 0.1		10:59:17.45	−30:36:57.5	3.263 ± 0.022 **Q**	VLT	7.6[n]	$8.1 \times 10^{27\,n}$
NVSS J111921−363139	18.7 ± 0.1	19.1	11:19:21.81	−36:31:39.1	2.768 ± 0.006	VLT	43.2[n]	$6.1 \times 10^{28\,n}$
NVSS J112641−383950	20.3 ± 0.3		11:26:41.00	−38:39:53.5	1.856 ± 0.003	VLT	9.4[n]	$3.2 \times 10^{27\,n}$
NVSS J120839−340307	18.0 ± 0.1	17.7	12:08:39.75	−34:03:09.6	1.120 ± 0.002	NTT	111.3	9.0×10^{27}
NVSS J122553−382823	19.2 ± 0.2		12:25:53.43	−38:28:26.2	continuum	VLT		
NVSS J140022−344411	16.3 ± 0.2	16.1	14:00:23.01	−34:44:11.3	0.7844 ± 0.0007	NTT	64.1	2.5×10^{26}
NVSS J140223−363539	19.8 ± 0.3	19.9	14:02:23.63	−36:35:42.2	2.796 ± 0.012	VLT	25.6[n]	$5.0 \times 10^{27\,n}$
NVSS J140854−382731	16.9 ± 0.2	16.6	14:08:55.24	−38:27:38.7	0.870 ± 0.003	NTT	43.3[n]	$4.2 \times 10^{26\,n}$
NVSS J141428−320637	15.5 ± 0.2[e]	15.4	14:14:28.27	−32:06:38.7[c]	0.2775 ± 0.0008	2.3 m	6.7	4.4×10^{25}
NVSS J144206−345115	> 20.1		14:42:06.69	−34:51:15.6	2.750 ± 0.004 **Q**	VLT	7.2[n]	$2.9 \times 10^{27\,n}$
NVSS J144932−385657	19.8 ± 0.2		14:49:32.79	−38:56:57.5	2.149 ± 0.002	VLT	57.2[n]	$3.4 \times 10^{27\,n}$
NVSS J145913−380118	18.3 ± 0.1		14:59:12.99	−38:01:19.0	continuum	NTT		
NVSS J151020−352803	20.2 ± 0.2	20.5	15:10:20.84	−35:28:03.2	2.931 ± 0.006	VLT	28.4[n]	$5.2 \times 10^{27\,n}$
NVSS J151021−364253	20.1 ± 0.2		15:10:21.80	−36:42:54.1	continuum	VLT		
NVSS J151215−382220	17.2 ± 0.1		15:12:15.51	−38:22:21.7	continuum	2.3 m		
NVSS J151503−373511	17.3 ± 0.1		15:15:03.09	−37:35:12.2	continuum	NTT		
NVSS J152123−375708	19.3 ± 0.3		15:21:24.02	−37:57:10.2	1.530 ± 0.003 **Q**	VLT	31.0	6.3×10^{26}
NVSS J152435−352623	20.9 ± 0.5		15:24:35.41	−35:26:22.0	2.752 ± 0.007 **Q**	VLT	16.8[n]	$6.4 \times 10^{27\,n}$
NVSS J152445−373200	18.3 ± 0.1	18.6	15:24:45.37	−37:31:58.5	1.798 ± 0.008	NTT	95.6[n]	$1.4 \times 10^{27\,n}$
NVSS J152737−301459	17.6 ± 0.2		15:27:37.88	−30:14:58.6	0.969 ± 0.008	VLT	105.8	1.0×10^{27}
NVSS J152747−364218	19.6 ± 0.2		15:27:47.38	−36:42:18.4	obscured by star	VLT		
NVSS J152921−362209	15.7 ± 0.3[e]		15:29:21.77	−36:22:14.6[c]	obscured by star	2.3 m		
NVSS J202856−353709[i]	16.9 ± 0.1		20:28:56.77	−35:37:06.0	obscured by star	DB		
NVSS J202945−344812[i]	17.6 ± 0.1	17.3	20:29:45.82	−34:48:15.5	1.497 ± 0.002	DB	161.4[m]	$7.2 \times 10^{26\,m}$
NVSS J210814−350823	19.5 ± 0.5		21:08:14.46	−35:08:25.3	1.879 ± 0.002	VLT	50.3[n]	$3.3 \times 10^{27\,n}$
NVSS J212048−333214	19.1 ± 0.1		21:20:48.76	−33:32:14.4	continuum	NTT		
NVSS J213238−335318	19.8 ± 0.4		21:32:38.95	−33:53:18.9	2.900 ± 0.001	VLT	13.4[n]	$9.4 \times 10^{27\,n}$
NVSS J213434−302522	16.8 ± 0.2	16.7	21:34:34.20	−30:25:20.6	0.6819 ± 0.0005	NTT	57.5	1.2×10^{26}
NVSS J213637−340318	19.7 ± 0.2	19.6	21:36:37.39	−34:03:21.1	2.772 ± 0.002	VLT	25.6[n]	$7.2 \times 10^{27\,n}$
NVSS J215009−341052	19.6 ± 0.3		21:50:09.30	−34:10:52.4	continuum	VLT		
NVSS J215047−343616	17.4 ± 0.1		21:50:47.38	−34:36:17.5	continuum	NTT		
NVSS J215226−341606	18.3 ± 0.3	18.0	21:52:26.74	−34:16:06.2	1.277 ± 0.002	NTT	180.0	7.7×10^{26}
NVSS J215455−363006	17.7 ± 0.1	16.9	21:54:55.08	−36:30:06.8	1.235 ± 0.001	NTT	43.7	3.4×10^{27}
NVSS J221104−351829	19.0 ± 0.2		22:11:05.04	−35:18:28.8	continuum	VLT		
NVSS J223101−353227	19.5 ± 0.2		22:31:01.72	−35:32:28.8	1.834 ± 0.006 **Q**	VLT	23.2	2.3×10^{27}
NVSS J223111−371459	17.6 ± 0.1	17.3	22:31:11.09	−37:14:59.9	1.248 ± 0.002	NTT	20.4	7.2×10^{26}
NVSS J223305−365658	16.6 ± 0.1	16.3	22:33:05.08	−36:56:58.2	0.939 ± 0.002	NTT	35.1	7.5×10^{26}
NVSS J225719−343954[i]	16.7 ± 0.1	16.5	22:57:19.63	−34:39:54.6	0.726 ± 0.001	DB	<43.5[m]	$1.4 \times 10^{26\,m}$
NVSS J230004−304711	17.4 ± 0.1	16.9	23:00:04.31	−30:47:08.7	0.5445 ± 0.0006	NTT	97.5	7.6×10^{25}
NVSS J231727−352606[h]	> 20.7		—	—	3.874 ± 0.002	DB	28.7[m]	1.4×10^{28}
NVSS J232125−375829	17.9 ± 0.1		23:21:25.55	−37:58:30.7	2.204 ± 0.006 **Q**	NTT	<8.4[n]	$4.0 \times 10^{27\,n}$
NVSS J233034−330009	17.2 ± 0.3[l]	17.1	23:30:34.49	−33:00:11.5	2.675 ± 0.005	NTT	123.5[n]	$6.4 \times 10^{27\,n}$
NVSS J233226−363423	17.9 ± 0.1		23:32:25.96	−36:34:24.1	0.988 ± 0.003 **Q**	NTT	85.1	3.3×10^{26}
NVSS J233627−324323	18.5 ± 0.1		23:36:27.09	−32:43:21.8	undetected	NTT		
NVSS J234145−350624[i]	16.9 ± 0.1	16.2	23:41:45.85	−35:06:22.2	0.644 ± 0.001	DB	<34.5[m]	$3.4 \times 10^{27\,m}$

[a] Two NVSS sources have been shown to be the components of one radio source

[b] SuperCOSMOS UKR optical position

[c] 2MASS (Skrutskie et al. 2006) position

[e] 2MASS K magnitude in 8-arcsec aperture

[h] This source was observed by De Breuck et al. (2004) in the SUMSS–NVSS sample with a K-band non-detection. We have reobserved it and improved the limit on the K-band non-detection.

[i] These sources were also part of the SUMSS–NVSS sample. The K-band magnitudes and positions given are from De Breuck et al. (2004).

[l] This object is at the position where the redshift was measured, but it may be a foreground star (see Section 3.1).

[m] Spectral indices used in calculating the luminosities are from Klamer et al. (2006) and the linear sizes are derived from LAS measurements either in De Breuck et al. (2004) or Klamer et al. (2006).

[n] Linear size is based on the largest angular size at 4800 or 8640 MHz. Luminosity was calculated using the 7-point spectral index (including 4800- and 8640-MHz data) from Paper II (table 3).

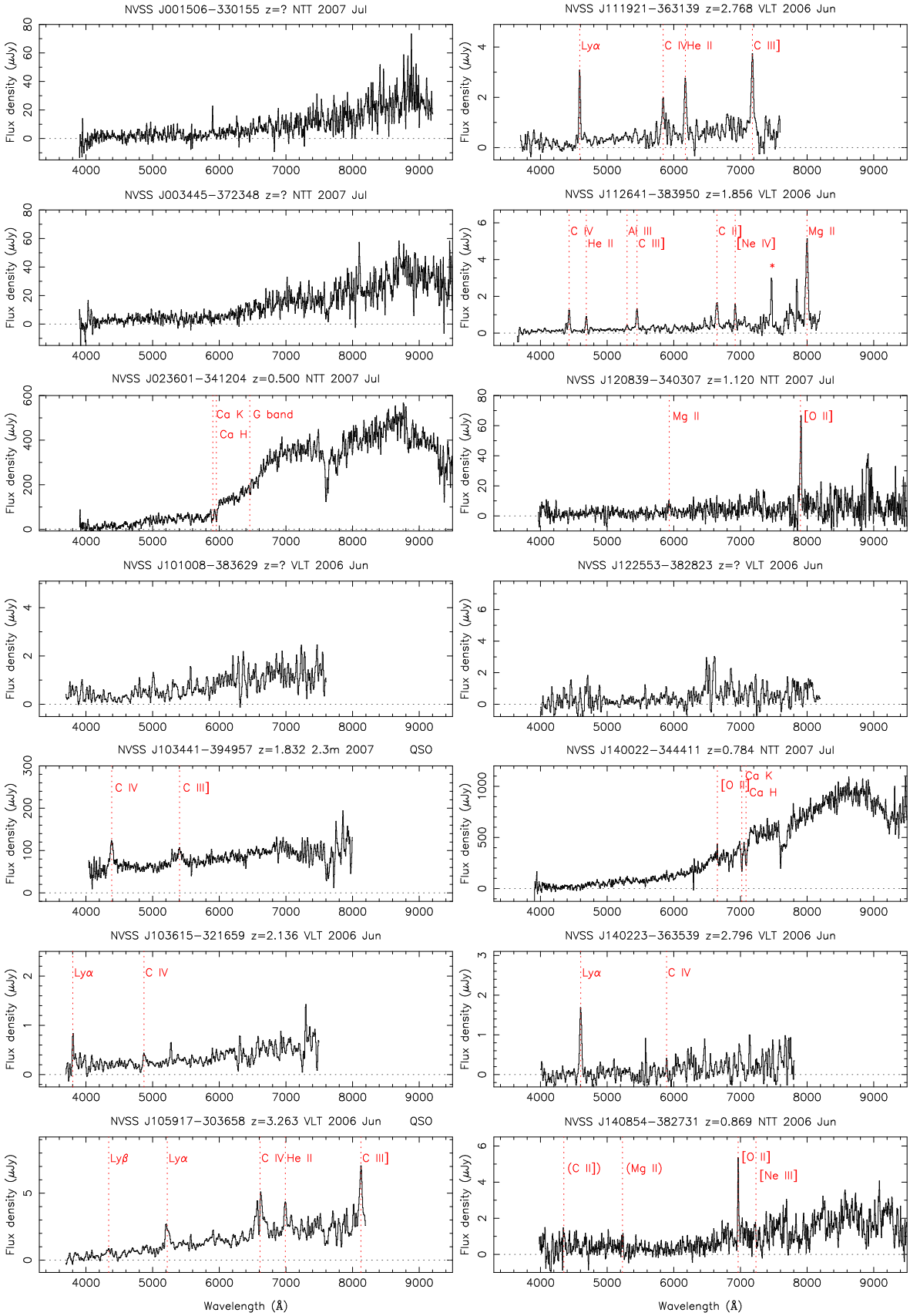

Figure 1. Spectra of sources with prominent features indicated. The source name, redshift and observing run are shown on top of each spectrum. The zero level is indicated by the horizontal dotted line. The positions of the vertical dotted lines indicate the predicted wavelengths of the lines at the redshift shown and not the wavelength of the fitted peak. Parentheses mark marginal detections of lines at the measured redshift and CR represents a cosmic ray. An asterisk shows the λ1305 O I+Si II line appearing in second order.

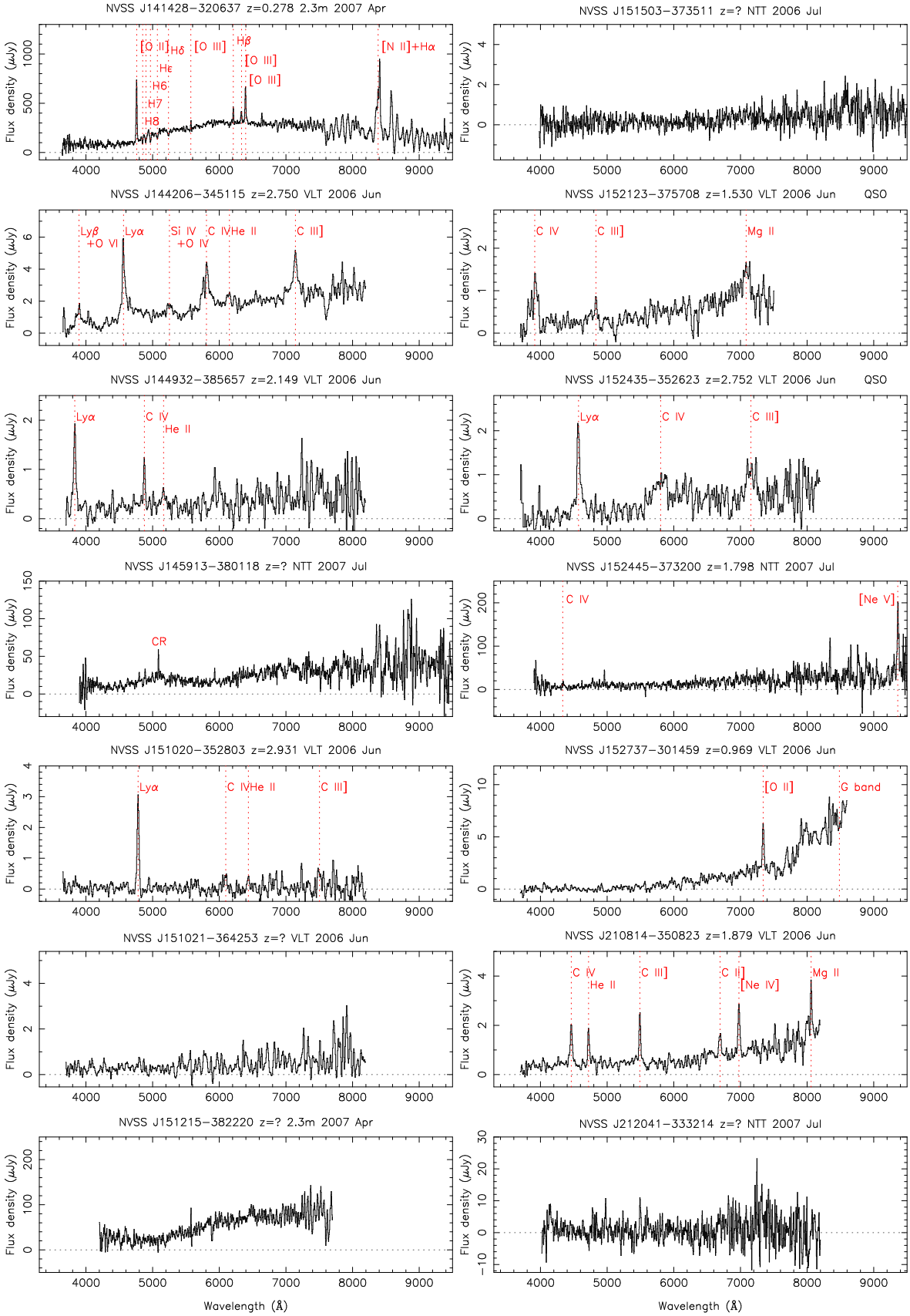

Figure 1 – *continued*

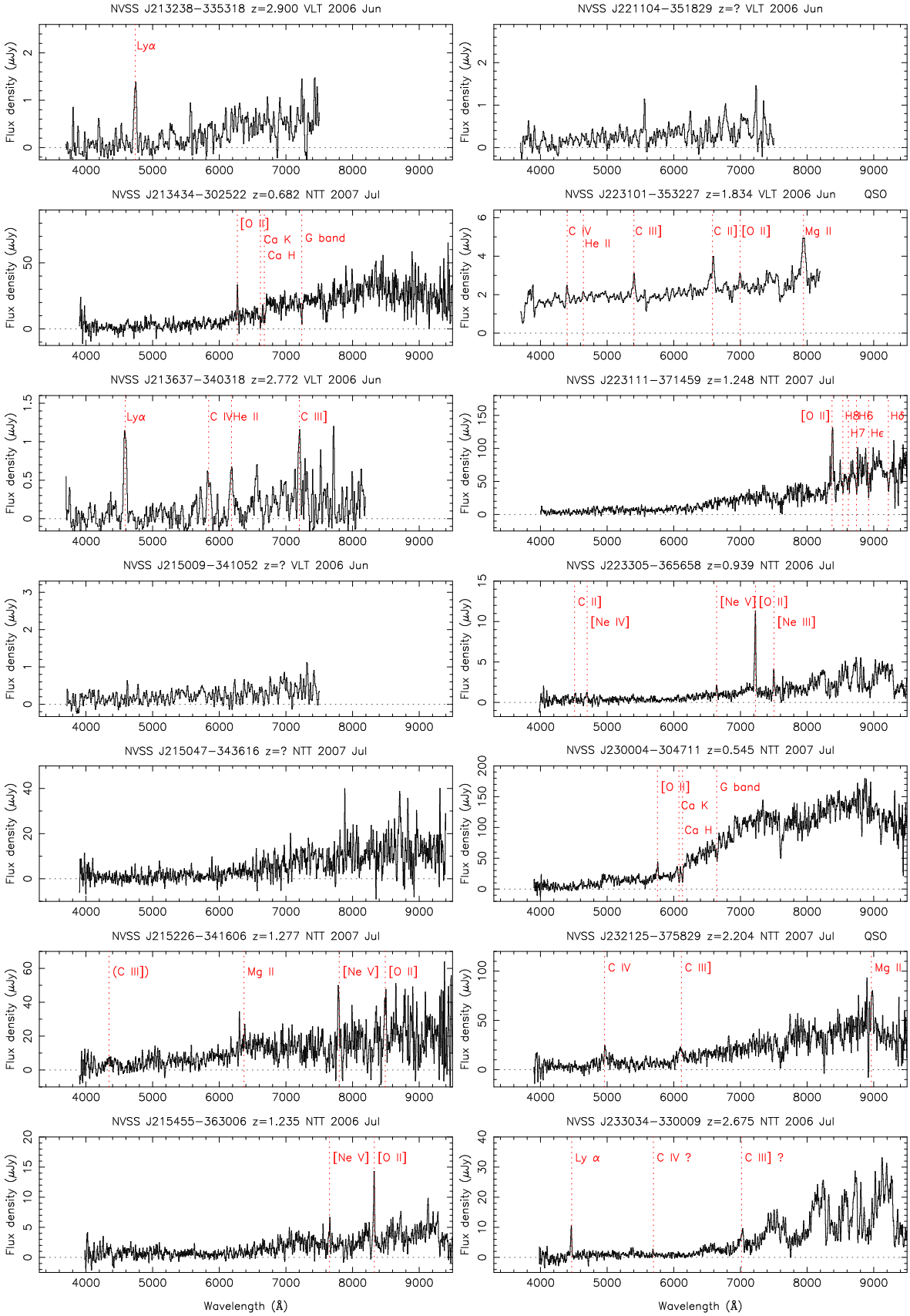

Figure 1 – *continued*

Table 3. Emission line measurements.

Source	z	Line	$\lambda_{\rm obs}$ (Å)	$\Delta v_{\rm FWHM}$ (km s^{-1})	Flux ($\times 10^{-16}$ erg s^{-1} cm^{-2})
NVSS J103441−394957	1.832 ± 0.008	C IV λ1549	4389.0 ± 1.2	6350 ± 700	162 ± 40
		C III] λ1909	5368.4 ± 9.7	14900 ± 5000	99 ± 25
NVSS J103615−321659	2.136 ± 0.012	Ly α λ1216	3803.0 ± 0.3	< 1700	0.85 ± 0.21
		C IV λ1549	4871.3 ± 0.5	1580 ± 160	0.30 ± 0.08
NVSS J105917−303658	3.263 ± 0.022	Ly β λ1026	4341.1 ± 3.4	7500 ± 1000	1.6 ± 0.4
		Ly α λ1216	5219.8 ± 1.0	4200 ± 300	1.9 ± 0.5
		C IV λ1549	6611.4 ± 2.6	7300 ± 600	2.6 ± 0.6
		He II λ1640	6991.2 ± 0.4	1300 ± 80	1.3 ± 0.3
		C III] λ1909	8124.8 ± 0.9	1600 ± 170	1.5 ± 0.4
NVSS J111921−363139	2.768 ± 0.006	Ly α λ1216	4588.6 ± 0.1	270 ± 20	1.8 ± 0.5
		C IV λ1549	5841.1 ± 0.7	2700 ± 180	1.4 ± 0.3
		He II λ1640	6173.8 ± 0.4	1450 ± 90	0.9 ± 0.2
		C III] λ1909	7179.3 ± 0.6	1200 ± 130	0.9 ± 0.2
NVSS J112641−383950	1.856 ± 0.003	C IV λ1549	4429.8 ± 0.1	750 ± 40	0.6 ± 0.2
		He II λ1640	4687.4 ± 0.2	480 ± 60	0.4 ± 0.1
		Al III] λ1858	5299.7 ± 1.3	1100 ± 400	0.05 ± 0.03
		C III] λ1909	5448.4 ± 0.1	810 ± 30	0.4 ± 0.1
		C II] λ2326	6647.2 ± 0.4	1270 ± 90	0.4 ± 0.2
		[Ne IV] λ2423	6921.2 ± 0.5	< 930	0.15 ± 0.04
		Mg II λ2798	7998.0 ± 0.3	1120 ± 70	0.9 ± 0.2
NVSS J120839−340307	1.120 ± 0.002	Mg II λ2798	5932.7 ± 0.8	1750 ± 450	5.2 ± 3
		[O II] λ3727	7906.7 ± 0.4	800 ± 100	7.5 ± 4
NVSS J140022−344411	0.7844 ± 0.0007	[O II] λ3727	6652.4 ± 0.3	< 470	7.6 ± 4
NVSS J140223−363539	2.796 ± 0.012	Ly α λ1216	4603.6 ± 0.3	1630 ± 100	0.9 ± 0.2
		C IV λ1549	5892.1 ± 0.3	< 1100	0.06 ± 0.03
NVSS J140854−382731	0.870 ± 0.003	[O II] λ3727	6966.4 ± 0.2	470 ± 90	0.79 ± 0.4
		[Ne III] λ3869	7214.3 ± 1.9	1580 ± 700	0.57 ± 0.3
NVSS J141428−320637	0.2775 ± 0.0008	[O II] λ3727	4759.8 ± 0.1	660 ± 50	125 ± 30
		[O III] λ4363	5576.2 ± 0.1	< 480	5.7 ± 3
		Hβ λ4861	6209.9 ± 0.1	110 ± 50	16.9 ± 4
		[O III] λ4959	6331.6 ± 0.4	560 ± 200	13.2 ± 3
		[O III] λ5007	6393.5 ± 0.1	470 ± 50	49.9 ± 10
		[N II] λ6583 + Hα λ6562	8392.5 ± 0.5	2500 ± 100	180 ± 45
NVSS J144206−345115	2.750 ± 0.004	Ly β λ1025 + O VI λ1034	3896.2 ± 2.3	8200 ± 900	2.6 ± 0.6
		Ly α λ1216	4563.8 ± 0.1	2840 ± 50	6.1 ± 1.5
		Si IV 1400 + O IV] λ1402	5252.5 ± 2.3	6100 ± 700	1.1 ± 0.3
		C IV λ1549	5808.1 ± 1.2	6800 ± 300	2.8 ± 0.7
		He II λ1640	6153.0 ± 9.2	5800 ± 2000	0.3 ± 0.1
		C III] λ1909	7142.3 ± 1.0	5600 ± 200	1.8 ± 0.4
NVSS J144932−385657	2.149 ± 0.002	Ly α λ1216	3832.1 ± 0.2	2730 ± 70	1.9 ± 0.5
		C IV λ1549	4876.0 ± 0.2	390 ± 50	0.4 ± 0.1
		He II λ1640	5164.6 ± 6.4	4700 ± 2000	0.26 ± 0.06
NVSS J151020−352803	2.931 ± 0.006	Ly α λ1216	4782.2 ± 0.1	1340 ± 40	1.4 ± 0.3
		C IV λ1549	6097.8 ± 2.2	1700 ± 500	0.11 ± 0.03
		He II λ1640	6436.9 ± 0.9	1330 ± 200	0.11 ± 0.03
		C III] λ1909	7503.5 ± 0.5	1110 ± 100	0.25 ± 0.06
NVSS J152123−375708	1.530 ± 0.003	C IV λ1549	3913.6 ± 1.2	8900 ± 400	3.5 ± 0.9
		C III] λ1909	4831.5 ± 0.6	2600 ± 200	0.6 ± 0.2
		Mg II λ2798	7084.8 ± 2.5	5700 ± 500	1.3 ± 0.3
NVSS J152435−352623	2.752 ± 0.007	Ly α λ1216	4571.5 ± 0.3	4430 ± 100	3.1 ± 0.8
		C IV λ1549	5803.0 ± 6.1	15800 ± 1500	2.5 ± 0.6
		C III] λ1909	7157.7 ± 3.8	7700 ± 800	1.8 ± 0.4
NVSS J152445−373200	1.798 ± 0.008	C IV λ1549	4334.7 ± 0.6	1530 ± 400	9.5 ± 5
		[Ne V] λ3345	9363.4 ± 0.4	740 ± 100	20.8 ± 10
NVSS J152737−301459	0.969 ± 0.008	[O II] λ3727	7341.0 ± 0.3	340 ± 70	0.61 ± 0.15

brightness of the object and the presence of a significant continuum make it unlikely to be at high redshift.

NVSS J152123−375708: A QSO with broad C IVλ1549.

NVSS J152435−352623: Three broad lines including a very broad C IVλ1549 line of 15800 km s^{-1} FWHM confirm that this is a QSO.

NVSS J213238−335318: The redshift is based on a single emission line, which we identify as Lyα, based on the absence

Table 3 – *continued*

Source	z	Line	$\lambda_{\rm obs}$ (Å)	$\Delta v_{\rm FWHM}$ (km s^{-1})	Flux ($\times 10^{-16}$ erg s^{-1} cm^{-2})
NVSS J210814−350823	1.879 ± 0.002	C IV λ1549	4462.1 ± 0.3	1730 ± 100	0.9 ± 0.2
		He II λ1640	4721.2 ± 0.2	830 ± 70	0.7 ± 0.2
		C III] λ1909	5491.1 ± 0.1	< 1200	0.5 ± 0.1
		C II] λ2326	6694.1 ± 0.6	1340 ± 130	0.24 ± 0.06
		[Ne IV] λ2423	6977.5 ± 0.4	900 ± 80	0.4 ± 0.1
		Mg II λ2798	8060.1 ± 0.4	< 800	0.4 ± 0.2
NVSS J213238−335318	2.900 ± 0.001	Ly α λ1216	4740.6 ± 0.5	2100 ± 200	0.97 ± 0.2
NVSS J213434−302522	0.6819 ± 0.0005	[O II] λ3727	6273.1 ± 0.2	310 ± 90	3.6 ± 2
NVSS J213637−340318	2.772 ± 0.002	Ly α λ1216	4587.9 ± 0.6	2700 ± 200	1.0 ± 0.2
		C IV λ1549	5841.4 ± 1.3	2850 ± 300	0.44 ± 0.1
		He II λ1640	6184.1 ± 0.9	2580 ± 200	0.4 ± 0.1
		C III] λ1909	7201.6 ± 0.7	1260 ± 140	0.29 ± 0.07
NVSS J215226−341606	1.277 ± 0.002	Mg II λ2798	6383.2 ± 0.4	280 ± 100	2.7 ± 1
		[Ne V] λ3426	7789.1 ± 0.7	800 ± 200	4.3 ± 2
		[O II] λ3727	8492.0 ± 0.9	970 ± 300	6.0 ± 3
NVSS J215455−363006	1.235 ± 0.001	[Ne V] λ3426	7659.1 ± 0.1	< 410	0.85 ± 0.4
		[O II] λ3727	8323.3 ± 0.4	480 ± 100	0.89 ± 0.4
NVSS J223101−353227	1.834 ± 0.006	C IV λ1549	4400.7 ± 0.6	1060 ± 200	0.34 ± 0.08
		He II λ1640	4644.3 ± 1.5	1300 ± 500	0.14 ± 0.03
		C III] λ1909	5402.2 ± 0.8	2060 ± 200	0.6 ± 0.1
		C II] λ2326	6580.6 ± 1.4	3690 ± 300	1.0 ± 0.2
		[O II] λ2470	6995.8 ± 0.6	1070 ± 120	0.30 ± 0.07
		Mg II] λ2798	7945.5 ± 0.9	2850 ± 200	1.3 ± 0.3
NVSS J223111−371459	1.248 ± 0.002	[O II] λ3727	8380.7 ± 0.4	790 ± 100	11.2 ± 3
NVSS J223305−365658	0.939 ± 0.002	C II] λ2326	4519.2 ± 1.3	1650 ± 800	0.59 ± 0.3
		[Ne IV] λ2423	4691.9 ± 3.3	2700 ± 2000	0.67 ± 0.3
		[Ne V] λ3426	6643.5 ± 0.6	670 ± 200	0.28 ± 0.1
		[O II] λ3727	7222.2 ± 0.1	680 ± 50	1.39 ± 0.7
		[Ne III] λ3869	7500.9 ± 0.4	520 ± 100	0.40 ± 0.2
NVSS J230004−304711	0.5445 ± 0.0006	[O II] λ3727	5755.3 ± 0.8	1340 ± 400	7.5 ± 4
NVSS J232125−375829	2.204 ± 0.006	C IV λ1549	4972.8 ± 0.5	2970 ± 300	42 ± 10
		C III] λ1909	6103.4 ± 4.0	5000 ± 2000	11.5 ± 3
		Mg II λ2798	8975.8 ± 0.8	830 ± 200	5.1 ± 2
NVSS J233034−330009	2.675 ± 0.005	Ly α λ1216	4461.7 ± 0.3	960 ± 200	4.4 ± 2
		C III] λ1909 ?	5687.8 ± 0.2	< 550	0.52 ± 0.3
		C IV λ1549 ?	7017.2 ± 3.8	4200 ± 1500	3.9 ± 2
NVSS J233226−363423	0.988 ± 0.003	Mg II λ2798	5576.1 ± 10	10700 ± 500	19.2 ± 5
		[O II] λ3727	7400.1 ± 1.3	2000 ± 500	11.2 ± 3

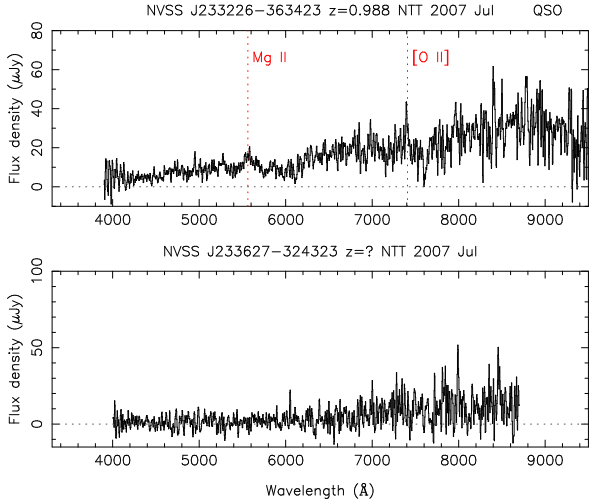

Figure 1 – *continued*

of blueward continuum emission. The bright line is spatially extended over 1.8 arcsec, supporting the Lyα identification.
NVSS J223101−353227: The C II]λ2326 and Mg IIλ2798 lines are broad, so we classify this object as a QSO. The line ratios support this interpretation (see section 4.5), though the line equivalent widths are unusually small for a QSO.
NVSS J223111−371459: The spectrum shows both [O II]λ3727 emission and strong Balmer absorption indicative of an A-star population.
NVSS J232125−375829: A quasar. The blue end of the spectrum is noisy and has been truncated but Lyα is not detected.
NVSS J233034−330009: From our original 1384- and 2368-MHz radio images, we initially chose the identification to be the bright K-band object between the lobes and closer to the stronger lobe. We had taken a spectrum of this object before the 4800-MHz-high-resolution image (shown in Paper II) identified a possible core which is 4-arcsec east of the bright K-band object. The spectrum is typical of an M-star, but there is a clear emission line in the blue which we identify as Lyα at a redshift of 2.675. The slit position angle was 165° and centred on the bright object and therefore does not go through the core position. The spatial profile of the Lyα line, shown in Fig. 2, is extended with a FWHM of 7.4 arcsec (60 kpc) along the slit. We therefore believe that the correct K-band identification is fainter than the limit on the IRIS2 image (i.e. $K > 19$) and that it is surrounded by a Lyα halo which extends from the core to beyond the bright source, which is an M star. In Fig. 3, we show the possible position of the Lyα halo. In a simplistic picture, where the Lyα halo is spherical, the 7.4-arcsec FWHM of the emission line at the slit can be reproduced by a halo of diameter ~ 10.5 arcsec, or 85 kpc. With an alternate geometry, the halo size would need to be a minimum of 32 kpc, the projected distance from the core to the bright object. This is a modest size for a Lyα halo, as some have been found to be > 100 kpc (Kurk et al. 2000a; Venemans et al. 2002; Reuland et al. 2007). Since the possible core was not detected in our 8640-MHz image this interpretation is open to question.

An alternative picture is that the bright K-band object is a galaxy and star coincident along the line of sight, and the middle component is a hotspot along the eastern jet. If this picture is correct then there is a marginal line at the wavelength expected for C IVλ1549. A further line sits at the expected position of C III]λ1909, but it cannot be differentiated from the M-star features at that wavelength.
NVSS J233226−363423: A very broad Mg IIλ2798 line, with a FWHM of 10^4 km s^{-1} indicative of a QSO.

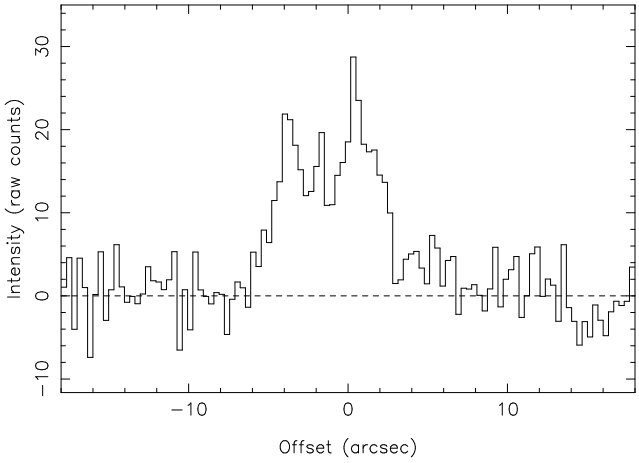

Figure 2. Spatial profile (north-south, positive offsets to the north) of the Lyα line in the NTT spectrum of NVSS J233034−330009. Lyα covers a FWHM of 7.4 arcsec or 60 kpc.

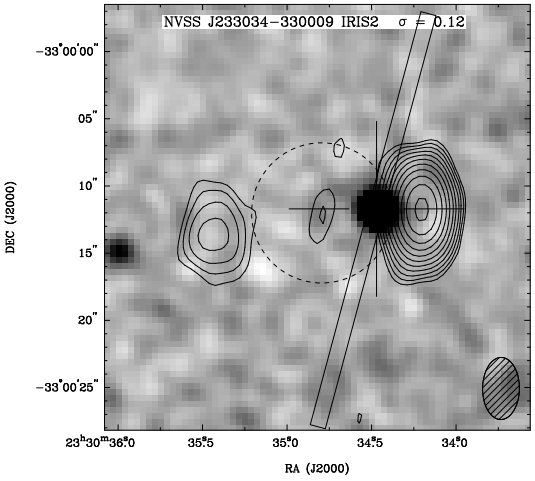

Figure 3. Our proposed model for NVSS J233034−330009 (see Section 3.1) drawn on the overlay of the 4800-MHz ATCA contours on the smoothed K-band image. The lowest contour is 3 sigma, and the contours are a geometric progression in $\sqrt{2}$. The rms noise (σ) is shown in the header in mJy beam^{-1}. The parallel lines represent the slit orientation (position angle of 165°) through the bright source (with cross-hairs), assumed to be a star. The dashed circle is the proposed Lyα halo, centred on the radio core, and with a diameter chosen to reproduce the observed width of the Lyα emission at the slit (7.4 arcsec), giving a halo diameter of 10.5 arcsec or 85 kpc.

4 DISCUSSION

4.1 K−z distribution

4.1.1 Emission-line contribution to K-band magnitudes

Strong emission lines such as [O II]λ3727 , [O III]$\lambda\lambda$4959, 5007 and Hα λ6562 can be shifted into the K-band, particularly at redshifts beyond $\sim$ 2. The contribution of these lines to the K-band magnitude is primarily dependent on redshift, but also on radio luminosity, due to the correlation between emission-line and radio luminosities (Willott

et al. 1999). Jarvis et al. (2001) calculated the emission-line contamination at each redshift for different 151-MHz flux densities. Adopting their approach, we have estimated the emission-line contamination to our K-band magnitudes for the MRCR–SUMSS sources. Firstly, we extrapolated our radio spectrum to 151 MHz, using the spectral index from our 5-point fit or, when unavailable, using the 843–1400-MHz spectral index (see Paper II). Some of the sources have a measured 151-MHz flux density (see Table 5) which was used. We then estimated the K-band contribution from emission lines using the information from Jarvis et al. (2001, fig.2), and then subtracted the emission-line contribution from the measured K flux. We find that in all but one case (NVSS J144932−385657) the typical contribution of the emission lines is less than the errors on our K magnitudes. The inherent assumptions in this process mean that a typical emission-line contamination was calculated, rather than an actual emission-line contribution. These assumptions include using average line ratios, the generalisation of the correlation between emission-line and radio luminosity, and the assumption that our radio spectra remain straight down to 151 MHz.

The only source where line emission may contribute to the K flux is NVSS J144932−385657 at $z = 2.149$, where the emission lines of [N II]λ6583 and Hα fall in the K band. This source is relatively faint at $K = 19.8 \pm 0.2$ and the possible emission-line contribution may account for up to 0.4 magnitudes of K-band flux. However, the spectrum in Fig. 1 shows that the emission lines are weak and therefore the lines that are shifted into the K-band may not have the maximum flux calculated here. Furthermore, this object is not an outlier in the K–z distribution (see Fig. 4 below) so there is no evidence that emission lines have boosted its K magnitude.

4.1.2 Trends on the K–z correlation

The K–z correlation is an empirical relationship that spans redshifts up to $z > 4$. While the correlation remains linear[3], different galaxy samples have been shown to give different linear fits to the K–z relation. Willott et al. (2003) made a fit to 64-kpc-aperture magnitudes based on the 3CRR, 6CE, 7C and 7CRS galaxy samples. The 3CRR sample was found to be ~ 0.6 magnitudes brighter in K at $z > 1$ than the 6C (Jarvis et al. 2001), while the 7C and 3CRR are offset in K-magnitude at all redshifts (Willott et al. 2003). A fit to the K–z relation for FIRST radio sources (El Bouchefry & Cress 2007) was also found to be fainter than the Willott et al. (2003) relation by more than 0.5 magnitudes at high redshift and even more at low redshift. These differences highlight the selection effects (including flux density limit) in any sample and show that the fits to the K–z plot depend on which samples are included and the aperture correction used. An individual fit, therefore, has no physical meaning but serves only to highlight whether a galaxy lies above or below the trend for that sample.

In Fig. 4 the 4-arcsec-aperture K magnitudes are plotted against redshift for all the sources in our sample that have spectroscopic redshifts, along with many samples from the literature with 4-arcsec-aperture K magnitudes. These are both USS-selected samples and non-USS-selected samples as listed in the Figure, and include the largest non-USS sample (McCarthy et al. 1996; 2007, private communication) comprising 277 K-band observations of radio galaxies, of which 175 have redshifts. The advantages of using the 4-arcsec-aperture magnitudes are discussed in Paper II and in terms of the K–z dispersion in Section 4.1.3. We have therefore chosen to adopt a fit to the 4-arcsec-aperture magnitudes from the combined literature samples as the most suitable metric that represents our data and allows more of the galaxies in our sample to be compared with the linear relation for HzRGs. For consistency with some papers in the literature we also show the K–z plot based on 64-kpc aperture values. The MRCR–SUMSS 64-kpc magnitudes are calculated from 8-arcsec-aperture magnitudes following the procedure described by Eales et al. (1997) and listed in Table 2.

Three fits to the 4-arcsec-aperture magnitudes in Figure 4 are shown. The fits are linear least-squares fits, because in each case the error on a quadratic fit was higher. QSOs and objects with contamination from foreground stars were not included in the fits. The equations of the fit lines are

$$K(4'') = 3.64\log(z) + 17.75 \quad (1)$$

for objects at all redshifts (solid line),

$$K(4'') = 3.45\log(z) + 17.76 \quad (2)$$

for $z > 0.6$ objects only (dotted line), and

$$K(4'') = 3.11\log(z) + 17.89 \quad (3)$$

for $z > 1.0$ objects (dashed line).

As the redshift range increases to include lower redshift objects, the fit steepens, whereas if the 4-arcsec aperture was missing any K-band flux we would expect the opposite effect, i.e., the fit would be flatter. There is therefore no compelling evidence that the lower redshift galaxies have K-band emission detected beyond a 4-arcsec aperture.

In Fig. 4 we have also plotted the evolutionary curves for elliptical galaxies with masses of $10^{11}\mathrm{M}_{\odot}$ and $10^{12}\mathrm{M}_{\odot}$ from the models of Rocca-Volmerange et al. (2004). The majority of identifications in our sample are consistent with elliptical galaxies of mass $10^{11} - 10^{12}\,\mathrm{M}_{\odot}$. Seymour et al. (2007) modelled HzRG masses from $H-$band magnitudes using early-type galaxy models from PEGASE2 (Fioc & Rocca-Volmerange 1997) with galaxy formation at $z = 10$ and a different initial mass function to that used by Rocca-Volmerange et al. (2004). Seymour et al. (2007) found that the majority of their galaxies fitted within the 10^{11}–$10^{11.5}$ $\mathrm{M}_{\odot}$ model over a redshift range of $1 < z < 4$.

The K–z distribution has a scatter about the fitted line due to the variations in stellar content of the galaxies, the amount of dust, and the rest wavelength range being sampled at each redshift. At high redshift UV light is observed in the near-IR, and this may introduce a contribution from the AGN continuum. In Fig. 4 there are two galaxies that are more than 2.5σ from the adopted best fit line (Eq. 1), and lie well outside the $10^{11}\mathrm{M}_{\odot}$ and $10^{12}\mathrm{M}_{\odot}$ model lines. NVSS J011606−331241 is 3.3σ fainter than the fit to the main distribution of points, with $K = 18.6$ and $z = 0.352$. This galaxy is in common with the SUMSS–NVSS sample;

[3] Linear fit between $\log(z)$ and K magnitude corresponds to a power-law relation between z and 2.2μm flux.

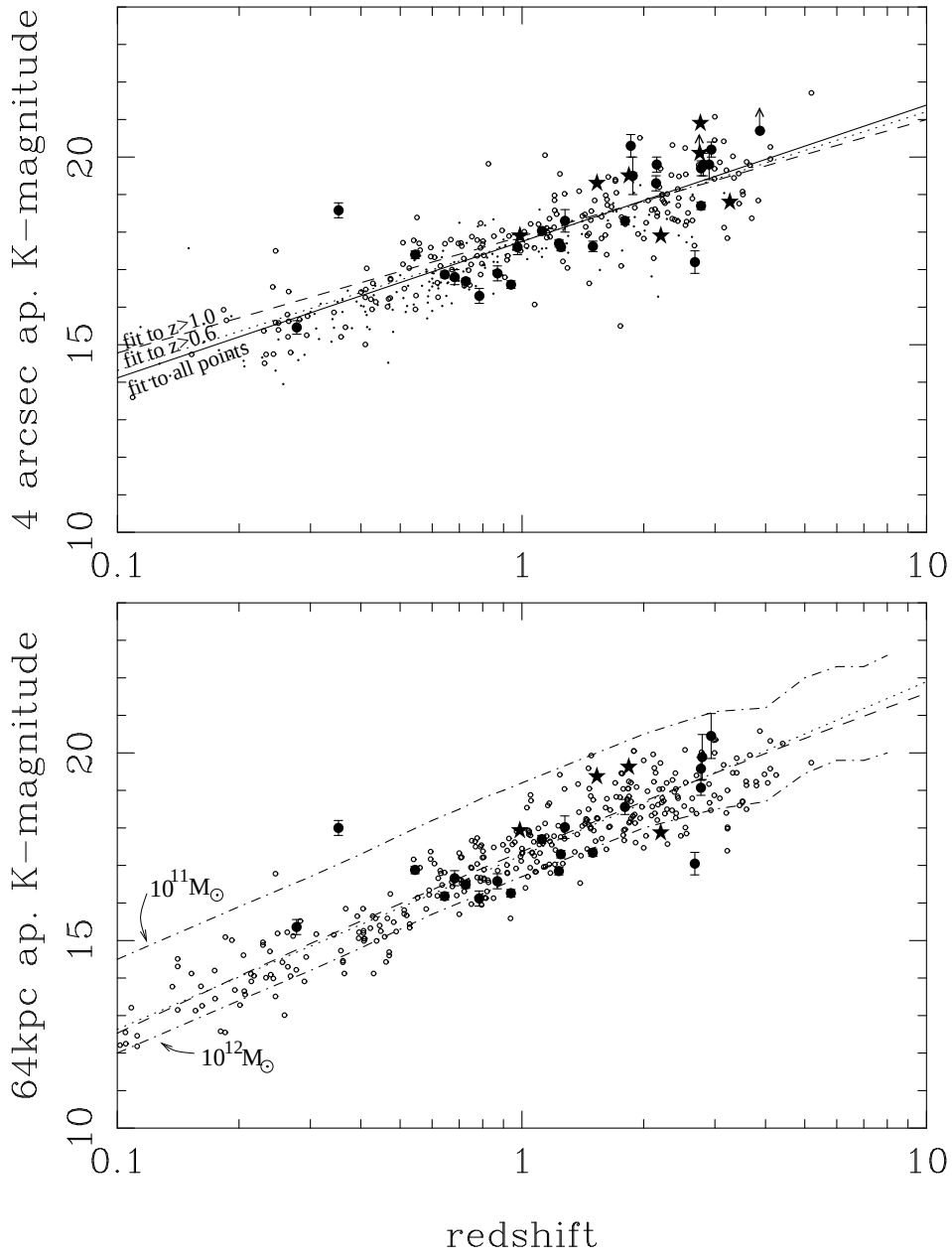

Figure 4. *Top*: K magnitudes in 4-arcsec apertures versus redshift for the MRCR–SUMSS HzRGs (filled circles), the MRCR–SUMSS QSOs (stars) and samples from the literature (small open circles). The literature samples were chosen because they had 4-arcsec K-band and redshift information. QSOs, uncertain redshifts, and lower limit K magnitudes were removed from the literature samples. Two of the samples (CENSORS, Brookes et al. 2006, 2008; and 6C**, Cruz et al. 2006) had 3- and 5-arcsec-aperture K magnitudes and a 4-arcsec-aperture magnitude was calculated by averaging the equivalent 3- and 5-arcsec fluxes and converting to a 4-arcsec magnitude. The other samples plotted are the 6C* from Jarvis et al. (2001), De Breuck et al. (2001, 2002) sample, 7C from Willott et al. (2003), SUMSS–NVSS from De Breuck et al. (2004, 2006) and the sample from Bornancini et al. (2007). The small dots are the McCarthy et al. (1996; 2007, private communication) sample in which the magnitudes were measured in a 3-arcsec aperture. Three straight line fits to both the literature samples and the MRCR–SUMSS sample are shown; a fit to points at all redshifts (solid line, Eq. 1), to points with $z > 0.6$ (dotted line, Eq. 2) and to points with $z > 1$ (dashed line, Eq. 3). The McCarthy points were not used in the fit calculations due to the smaller measurement aperture for that sample and neither were the QSOs and objects with contamination by a foreground star in the MRCR–SUMSS sample. The redshift errors for our MRCR–SUMSS data are much smaller than the plotted filled circle as are some of the K-magnitude errors. *Bottom*: K magnitudes in a 64-kpc metric aperture versus redshift for the MRCR–SUMSS HzRGs (filled circles), the MRCR–SUMSS QSOs (stars) and samples from the literature (small open circles). The literature samples are the 3CRR, 6CE, 6C* and 7CRS radio galaxy samples compiled by Willott et al. (2003), the composite samples of van Breugel et al. (1998) and De Breuck et al. (2002), the SUMSS–NVSS sample and the McCarthy sample. The 64-kpc aperture magnitudes for the MRCR–SUMSS, SUMSS–NVSS and McCarthy samples were calculated from 8-arcsec-aperture magnitudes (see text for limitations). We have also plotted the corresponding 64-kpc and 8-arcsec-aperture fit equations from Willott et al. (2003) (dashed line) and De Breuck et al. (2004) (dotted line) respectively. The dot-dash lines are the $10^{11}M_\odot$ and $10^{12}M_\odot$ elliptical galaxy evolution models from Rocca-Volmerange et al. (2004).

Table 4. The dispersion in the K-magnitude as a function of redshift for all the galaxies in Fig. 4 but excluding QSOs and galaxies that are contaminated by foreground stars. The number of galaxies in each redshift bin is given in brackets beside the dispersion.

Fit equation	Dispersion (mag)		
	all z's	$z < 2$	$z > 2$
64-kpc fit	0.7 (534)	0.7 (441)	0.9 (93)
all 4″ ap.	0.7 (211)	0.7 (146)	0.7 (65)
$z > 0.6$ for 4″ ap.	0.7 (211)	0.8 (146)	0.7 (65)
$z > 1.0$ for 4″ ap.	0.8 (211)	0.8 (146)	0.7 (65)

in De Breuck et al. (2006) it was concluded that there is a chance the correct identification may be a fainter nearby galaxy but higher resolution radio imaging is needed to confirm this. The other main outlier is NVSS J233034−330009 which is 2.8σ brighter than predicted, with $z = 2.675$ and $K = 17.2$; this source is discussed in detail in Section 3.1.

4.1.3 Dispersion in the K–z distribution

An increase in the dispersion of points on the K–z plot at high redshift has been used in the past to constrain the epoch of formation of radio galaxies. Eales et al. (1997) found an increase in dispersion above $z \sim 2$, and concluded that those galaxies were in the process of formation while those at $z < 2$ are evolving passively. On the other hand, Jarvis et al. (2001) found no evidence for an increase in the dispersion of K magnitudes at $z > 2$, and concluded that radio-luminous systems formed most of their stars at $z > 2.5$ and have evolved passively since then.

In Table 4, we have calculated the dispersion in redshift bins for all the galaxies in Fig. 4 based on each fit shown. This shows that the dispersion in the 64-kpc-aperture points around the Willott et al. (2003) fit is no lower than dispersion of the 4-arcsec-aperture points about the fit to all redshifts. Therefore, we have adopted the 4-arcsec-aperture metric with the fit in Eq. 1 in order to compare the MRCR–SUMSS galaxies with the trend in radio galaxies for the rest of this paper. There is no evidence for an increase in dispersion above $z = 2$ for the 4-arcsec-aperture fits. This supports the results found by Jarvis et al. (2001) and De Breuck et al. (2006) that radio galaxy hosts have been evolving passively since epochs corresponding to $z = 3$ or earlier.

4.1.4 QSOs in the MRCR-SUMSS sample

QSOs are usually removed from HzRG samples on the basis that their K-band flux is generated by the central AGN rather than from stellar light. The implication is that the non-thermal AGN flux would be stronger than the thermal contribution from the host and hence bias the K–z distribution in favour of brighter K-band magnitudes. The unification model of AGNs (Barthel 1989; Antonucci 1993; Urry & Padovani 1995) suggests that the difference between radio galaxies and radio-loud QSOs is an orientation effect, such that the QSOs are viewed so the nucleus can be seen directly rather than being obscured by a dusty torus as in a radio galaxy. QSOs would therefore be expected to have smaller apparent linear sizes. While Barthel (1989) found that QSOs, on average, were a factor of two smaller than radio galaxies, many QSOs have large radio linear sizes, up to several Mpc (Riley et al. 1989; Bhatnagar, Krishna & Wisotzki 1998; Paper II, section 3.2.1) and some do not show very bright central sources. Alternatively, it has been argued that the difference between QSOs and radio galaxies may be due instead to their evolutionary stage and/or environment. For instance, compact radio sources were found to live in denser environments than extended sources by Prestage & Peacock (1988) and this was used as an argument for them being different types of sources. It is possible, therefore, that radio morphology may depend more on the age or environment of a source than its viewing angle. As a result we consider it important to include QSOs in any follow-up study of HzRG environments.

It has been suggested that the alignment effect between radio structures and UV/optical light seen in HzRGs is also apparent in QSOs (Lehnert et al. 1999) and can be explained by scattering of light from the active nucleus rather than jet-induced star formation. Scattering models are favoured because the emission is highly polarised. While broad emission lines have long been the defining features of QSOs, the distinction between radio-loud QSOs and radio galaxies is not clear-cut. It is worth noting that compact steep-spectrum QSOs in the Molonglo Quasar Sample (Baker & Hunstead 1995) also have properties similar to HzRGs: a heavily reddened optical continuum, strong narrow forbidden lines and narrower than usual permitted lines. USS QSOs are quite rare, and therefore may have different physical characteristics to the bulk of the QSO population.

While our fits to the K–z plot do not include the QSOs, it can be seen in Figure 4 that the QSOs tend to fall on the *faint* side of the fit to all redshifts, indicating that the K-band flux is not unusually strong in comparison with the radio galaxies. If the QSOs had been included, the $z > 1$ fit does not change Eq. 3 within the precision shown. We note, however, that target selection for spectroscopic followup was based on K-band magnitude but not on K-band morphology; hence bright QSOs will not be included in our sample.

While the objects with line widths $> 3000\,\mathrm{km\,s^{-1}}$ have been classified as QSOs, we find no evidence from the K-band magnitudes that we are seeing the nuclear source directly. Furthermore, two of the MRCR–SUMSS QSOs — NVSS J223101−353227 and NVSS J233226−363423 — have extended K-band emission that is aligned (within 7- and 3-degrees respectively) with the radio structure.

In Fig. 5, we compare the MRCR–SUMSS radio galaxies and QSOs with the overall K–z fit for radio galaxies defined by 4-arcsec aperture magnitudes. The offsets between the measured redshifts and those predicted by Equation 1, z(fit)−z(spec), are plotted against radio luminosity, linear size and redshift. It is clear that the differences among the K–z fits defined by Eqs. 1, 2 and 3 are small in comparison to the scatter about each fit. Moreover, these QSOs do not stand out from the HzRGs in linear size, radio luminosity or redshift distribution. It is *only* the spectral line width that differentiates QSOs from HzRGs in the MRCR–SUMSS sample.

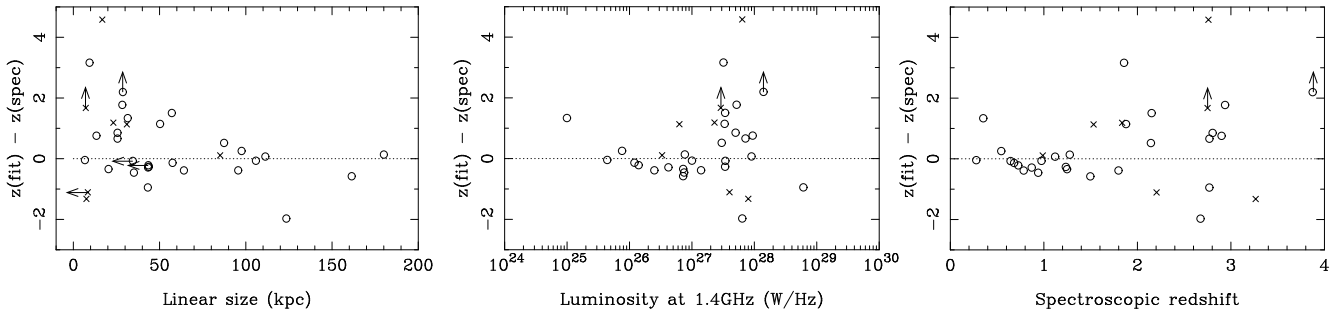

Figure 5. The difference between predicted and spectroscopic redshifts (where the predicted redshift comes from the K–z fit in Fig. 4, Eq 1) as a function of linear size, 1.4-GHz luminosity and spectroscopic redshift. Circles are radio galaxies and crosses mark the QSOs.

4.2 Linear size

In some USS-selected HzRG samples an explicit maximum radio angular size cut-off has been applied (see for example Blundell et al. 1998; De Breuck et al. 2000a), on the assumption that the higher-redshift sources are younger and hence smaller (Blundell, Rawlings & Willott 1999). Our plot of largest linear size versus redshift in Fig. 6 is limited by the small number of redshifts measured so far (21 per cent of K detections have redshifts). The selection of galaxies for redshift followup is likely to exclude some radio-extended but optically-faint objects (as discussed in Section 4.4.2) which we expect to be lower redshift dust-obscured galaxies that would populate the top left of Fig. 6. However, the upper envelope of source sizes drops at higher redshift. Linear size evolution is well known in radio samples (Kapahi, Subrahmanya & Kulkarni 1987; Barthel & Miley 1988), but Blundell et al. (2002) found only a weak correlation between redshift and linear size measured at low (74 MHz) frequency. The correlation here is also weak. Further analysis will be carried out when the spectroscopy for the MRCR–SUMSS sample is complete.

The measured $K-$magnitudes have also been plotted against largest angular size (LAS) in Fig. 7. Our adopted cosmology dictates that the LAS will change with redshift, and therefore a line is shown representing the LAS of a 50-kpc source at each redshift, and similarly for a 100-kpc source. In both cases, the LAS was calculated using our chosen cosmological parameters (see Section 1), and then the redshifts were converted to K magnitudes using Equation 1. If the distribution of points decreases faster than the lines marking the cosmological models, then more distant USS-selected galaxies may be intrinsically smaller than their low-redshift counterparts. The median LAS of our objects at each K magnitude generally decreases faster than the cosmological models. However, a Spearman rank test confirms there is no correlation in Fig. 7.

4.3 The alignment effect

Alignment between near-infrared and radio structures has been found in many HzRG samples, and these are discussed in detail in Paper II. However, the redshift dependence of the alignment effect is very much in dispute, with some investigations finding a clear increase in alignments with redshift (e.g. van Breugel et al. 1998), while others find no such trend (e.g. Pentericci et al. 1999). We now examine the redshift de-

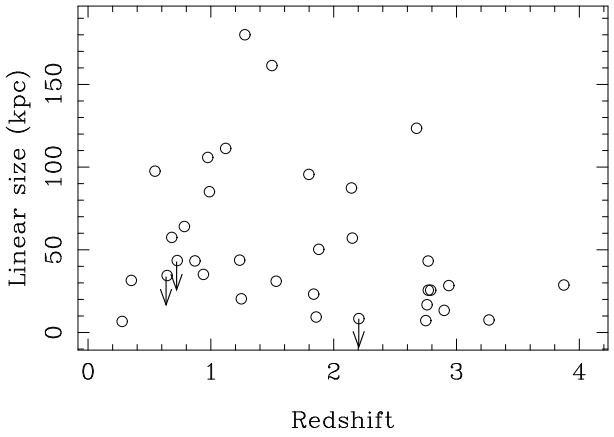

Figure 6. Largest linear size from Table 2 versus redshift for sources (excluding QSOs) in our sample with spectroscopic redshifts.

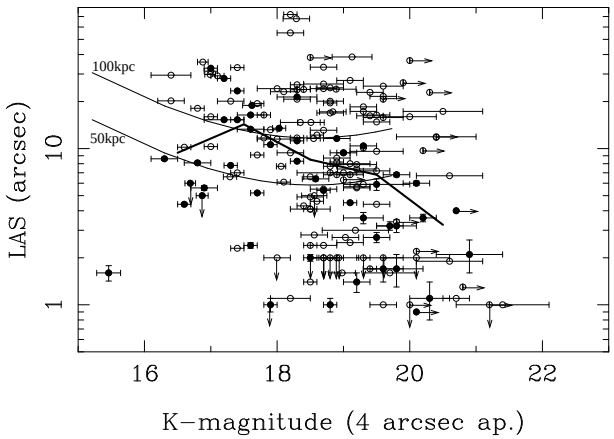

Figure 7. Largest angular size (LAS) versus 4-arcsec-aperture K magnitudes for the MRCR–SUMSS sample. The LAS was measured from the 4800- or 8640-MHz images (see Paper II, table 3) where available, and otherwise, the value comes from Paper II, table 2. Two solid curves represent the angular size of a 50-kpc- and 100-kpc-diameter galaxy versus redshift (based on Equation 1 from the K–z plot) for our adopted cosmological model. The heavier solid line joins points which are the median LAS values in each magnitude bin from 16–17 up to 20–21 magnitudes. Solid points represent the objects that were followed up with spectroscopy (irrespective of whether that resulted in a redshift measurement).

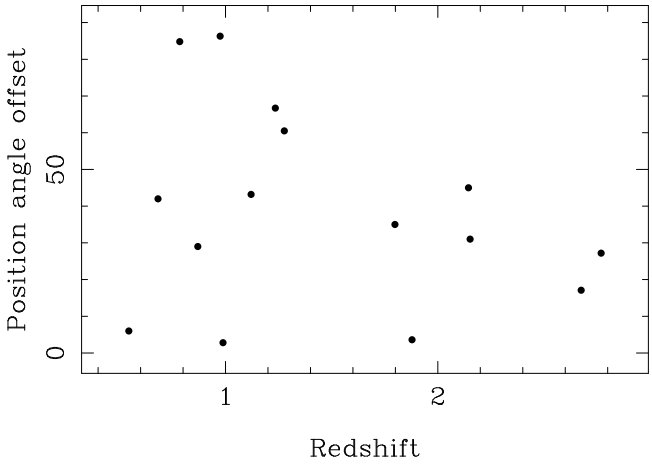

Figure 8. The offset between the radio axis position angle and that of the major axis of the ellipsoidal fit to the K-band galaxy versus redshift. Sources with LAS<5 arcsec are not included as the position angle offsets may be less accurate.

pendence of the alignment effect in the MRCR–SUMSS sample. In Paper II we fitted ellipsoidal profiles to the K-band host galaxies. The major axis of the ellipsoids was found to align with the radio structure in 21 per cent of the 122 galaxies for which an elliptical profile could be fitted. Fifteen of the 122 fitted galaxies have redshifts and they are plotted in Fig. 8 against the position angle offset, defined as the difference between the radio axis and the major axis of the fitted K-band ellipsoid. There may be an upper envelope to the distribution of points, which falls with increasing redshift. If that remains the case when the spectroscopic sample is complete, then it would imply that the higher-redshift objects show closer alignment than those at lower redshifts.

In Paper II we identified sources with alignment offsets of less than 10 degrees as being likely candidates for jet-induced star formation. Only three of those have redshifts in Fig. 8. While the trend with redshift identified here is clearly not associated with such highly aligned processes, larger position angle offsets have been attributed to ionisation cones or extended emission-line regions in some high redshift galaxies. Such features would not be seen in galaxies at $1.3 \leqslant z \leqslant 1.9$ where there are no bright emission lines in the K-band. It is noteworthy that the objects which are highly misaligned, including those with perpendicular axes (> 80 degrees), are all at low redshift.

4.4 The efficiency of low-frequency selection

4.4.1 Spectral curvature

The original purpose of selecting sources that are ultra-steep between 408–843 MHz was to test whether the sample would preferentially select higher redshifts than USS samples selected at higher frequencies. This would be the case if the radio spectrum steepens at higher frequencies and the steeper part is redshifted down to 408–843 MHz, in which case the lower-frequency selection would include fewer low-redshift objects. In Paper I we found that 85 per cent of USS-selected sources have straight radio spectra between 408–2368 MHz (observed frame) and therefore the frequency of USS selection should not affect the resultant sample if selected at a frequency higher than 408 MHz. Similarly Klamer et al. (2006) found that 89 per cent of a subsample of 37 sources from the SUMSS–NVSS sample also have straight radio spectra from 843 MHz to either 6.2, 8.6 or 18 GHz. However, Bornancini et al. (2007) found that the majority of their USS sample have radio spectra that flatten from 352 MHz to 74 MHz. If the radio spectrum remains straight over a larger frequency range, then the spectral index is independent of the observed frequency. In that case, the z–α correlation would not be due to a k-correction. The steep spectrum would instead be intrinsic to the source or the environment it is in.

We have an opportunity to investigate the shape of the radio spectrum below 408 MHz for the MRCR–SUMSS sample as some of the sources are also in the 74-MHz VLA Low-Frequency Sky Survey (VLSS; Cohen et al. 2007) and the 151-MHz Mauritius Radio Telescope (MRT) Southern Sky Survey (Pandey 2006). These two catalogues, while useful, have limitations. Firstly, the declination of our sources is at the southern edge of the VLSS survey region, where the flux densities are considered less reliable. Secondly, the large MRT beamwidth (4×4.8 arcmin at declination -35°) is subject to beam confusion. We note that the MRT flux density calibration is tied to interpolated 151-MHz flux densities for strong sources in the Burgess & Hunstead (2006) compilation. Errors in flux density were assumed to be the quadratic combination of a 0.26-Jy-rms noise plus confusion term and a 6.3 per cent scale uncertainty (Pandey 2006).

Inclusion of 74- and 151-MHz flux densities in our spectrum fits was done only after careful assessment of the radio images. MRT and VLSS images were overlaid with images from MRCR and SUMSS to check for confusion in the MRT images, and flux density or morphological anomalies in VLSS at these large zenith distances. The MRCR–SUMSS sample sources which have a reliable 74-MHz flux density have been fitted with a 6-point spectral index between 74 and 2368 MHz in Paper I (table 10) and those with a K-band counterpart are listed in Table 6. The 151-MHz catalogue does not cover all of our survey region, but we found matches to ten of the MRCR–SUMSS sources which have K-band counterparts. These are given in Table 5 along with a revised spectrum fit which includes the new frequency point. Two of these have both 74-MHz and 151-MHz flux densities. An example of the fit to one source is shown in Fig. 9.

In Tables 5 and 6, 75 per cent (15/20) of sources have spectral shapes that remain a power-law down to either 74 or 151 MHz. The mean K-band magnitudes are 17.9 and 18.0 for the flattening and straight-spectrum sources respectively. The difference between these distributions is not statistically significant (based on a Wilcoxon rank-sum test). Therefore, we find that the majority of our sources have a spectral shape that remains straight, which supports a picture in which the steep spectrum is intrinsic to high redshift sources and that a k-correction is not the reason why these high-redshift sources have been identified by our selection criteria.

4.4.2 Relationships among redshift, K, α and 1400 MHz flux density distributions

In Paper II we compared the K-band magnitude distribution of the MRCR–SUMSS sample to both USS-selected- and non-USS-selected-samples from the literature, and found that the resulting K-band distribution was independent of

Table 5. Sources from the MRCR–SUMSS sample which have a K-band identification and a 151-MHz flux density in the MRT catalogue. K magnitudes in a 4-arcsec aperture and the 151-MHz flux densities are listed. The spectral index is shown for sources with a power-law radio spectrum. All the spectral indices are 6-point values between 151 and 2368 MHz, except for NVSS J213238−335318 which has an 8-point index from 151 to 8640 MHz, NVSS J233729−355529 which has a 4-point index from 151 to 1400 MHz and NVSS J234145−350624 which has fluxes measured at 9 frequencies from 151 MHz to 18 GHz. Sources without spectral indices listed flatten towards lower frequencies. Objects which also have 74-MHz flux densities (Paper I, table 10) are marked with an asterisk, and the 74-MHz flux density was used in the spectral index fit.

Source	K (4-arcsec)	S_{151} (Jy)	α	Redshift
NVSS J003445−372348	17.0	2.77 ± 0.31	-1.20 ± 0.03	—
NVSS J202720−341150	> 20.3	2.39 ± 0.30	-1.13 ± 0.04	—
NVSS J213238−335318	19.8	1.32 ± 0.27	-1.41 ± 0.02	2.900
NVSS J214114−332307*	19.1	2.19 ± 0.29	flattening	—
NVSS J215455−363006	17.7	3.78 ± 0.35	-1.13 ± 0.03	1.235
NVSS J223305−365658	16.6	1.99 ± 0.29	-0.95 ± 0.04	0.939
NVSS J233535−343330	18.9	3.40 ± 0.34	-1.05 ± 0.03	—
NVSS J233729−355529	19.2	2.58 ± 0.31	-1.39 ± 0.05	—
NVSS J234145−350624	16.9	11.26 ± 0.76	flattening	0.644
NVSS J235945−330354*	19.1	2.76 ± 0.31	flattening	—

Table 6. Sources from the MRCR–SUMSS sample which have a 74-MHz flux density (from Paper I, table 10) and a K-band identification and are not already shown in Table 5. K magnitudes in a 4-arcsec aperture and the 74-MHz flux densities are listed. All the spectral indices are six-point values between 74 and 2368 MHz except for NVSS J230846−334810 which has a four-point fit between 74 and 1400 MHz. Sources without spectral indices listed flatten towards lower frequencies.

Source	K (4-arcsec)	S_{74} (Jy)	α	Redshift
NVSS J000231−342614	18.2	1.35 ± 0.19	-0.98 ± 0.04	—
NVSS J000742−304325	18.9	0.77 ± 0.10	flattening	—
NVSS J001506−330155	17.6	2.10 ± 0.24	-0.89 ± 0.03	—
NVSS J021759−301512	18.3	1.56 ± 0.17	-1.04 ± 0.03	—
NVSS J120839−340307	18.0	22.93 ± 2.34	-1.10 ± 0.03	1.120
NVSS J141428−320637	15.5[a]	3.78 ± 0.49	flattening	0.2775
NVSS J215047−343616	17.4	4.49 ± 0.53	-1.05 ± 0.03	—
NVSS J215226−341606	18.3	1.67 ± 0.22	-0.99 ± 0.03	1.277
NVSS J221650−341008	16.4	2.23 ± 0.29	-1.00 ± 0.03	—
NVSS J230846−334810	17.0	1.61 ± 0.20	-1.13 ± 0.04	—

[a] 2MASS magnitude in an 8-arcsec aperture.

the flux density distribution. Here we look at the redshift distribution of the same samples and we investigate any biases in the selection of objects for spectroscopic followup.

Fig. 10 shows the redshift and 1400 MHz flux density distributions for our MRCR–SUMSS sample and the SUMSS–NVSS, 6C** (Cruz et al. 2006), De Breuck et al. (2001, 2002), McCarthy et al. (1996; 2007, private communication), CENSORS (Brookes et al. 2006, 2008) and a combined sample from the 3CRR, 6C*, 6CE and 7CRS catalogues (compiled by Willott et al. 2003). The McCarthy and CENSORS samples were not USS-selected, while the Willott et al. sample is predominantly non-USS-selected apart from 23 sources from the 6C*. The McCarthy sample includes 175 redshifts from a set of 277 K-band observations of radio galaxies. It is the largest non-USS K-band sample even though it remains unpublished. The 1400 MHz flux density values for the McCarthy sample were obtained by cross-matching the positions with the NVSS catalogue within a 60-arcsec search radius. For sources which had two matches within 60 arcsec, we selected the closest match. SUMSS–NVSS was selected to have $\alpha_{843}^{1400} < -1.3$, and the 6C** sample is from the 151-MHz 6C survey with $\alpha_{151}^{1400} < -1.0$. The De Breuck et al. (2001, 2002) sample was selected at one of the frequencies 325, 365, or 408 MHz as detailed in the papers, and has $\alpha_{\sim 350}^{1400} \lesssim -1.3$. We have only included sources from the De Breuck et al. (2001, 2002) sample that have measured K magnitudes. The combined sample compiled by Willott et al. (2003) includes 202 narrow-line galaxies from the 3CRR, 6C*, 6CE and 7CRS catalogues, selected at 151 and 178 MHz. Spectroscopic redshifts are available for 193 (96 per cent) of those. The 1400 MHz flux densities were obtained from the NASA/IPAC Extragalactic Database (NED) by selecting the most recently published[4] integrated flux density. In several cases only peak flux densities were

[4] Flux densities came from Condon et al. (1998), Laing & Peacock (1980), Kellermann, Pauliny-Toth & Williams (1969), White & Becker (1992), Owen & Ledlow (1997), Croston et al. (2005) and Becker, White & Helfand (1995).

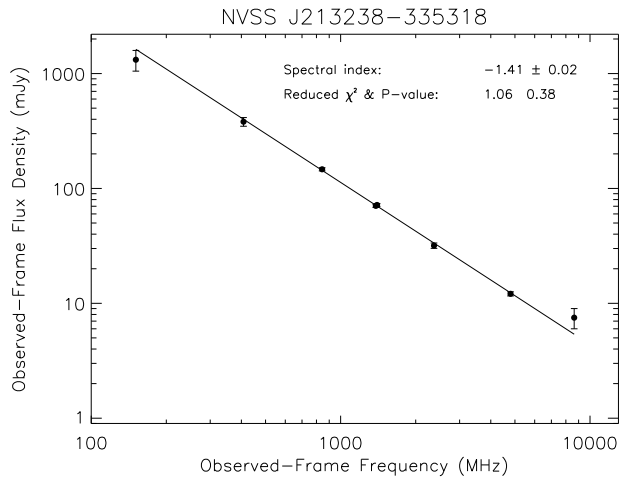

Figure 9. The observed-frame radio spectral energy distribution for NVSS J213238−335318 at $z = 2.900$. Of the sources in Tables 5 and 6, this source was fitted to a power-law using the largest frequency range, from 151 to 8640 MHz. The resultant spectral index and goodness-of-fit statistics are shown.

available and 25 targets (13 per cent) have no published observations at 1400 MHz. As the 3CRR/6C*/6CE/7CRS combined sample has nearly-complete redshift followup, the histograms shown in Fig. 10 are not biased compared to the corresponding K-band distributions in Paper II.

It is important to note that while the K-magnitude measurements are mostly complete for each of the USS samples, the redshifts are incomplete. The percentage of K-band detections with spectroscopic redshifts is 32 per cent for 6C**, 46 per cent for SUMSS–NVSS, 40 per cent for De Breuck et al. (2001, 2002) and currently 21 per cent for the present MRCR–SUMSS sample.

The choice of targets for follow-up spectroscopy in the MRCR–SUMSS sample was essentially determined by the telescope being used. On the one hand, the faintest objects are the best high-z candidates for followup spectroscopy, but the available telescope time will always limit the number of faint objects that can be observed. The brightest K-band objects were observed with the ANU 2.3 m, and those that were not detected were then observed on the NTT along with fainter targets down to $K \lesssim 19$. After the magnitude cut, the targets were then chosen on Right Ascensions available. The $K > 19$ objects were observed at the VLT, where we had a slight preference to observe the more compact objects, but this was also limited by the accessible Right Ascensions. To test whether the objects that have spectroscopy are representative of the whole sample, we distinguish them with different symbols in Fig. 7 which shows largest angular size of the sources versus K-band magnitude. While the distribution of the objects with spectra is similar to that for the full sample, among the faintest targets observed on the VLT there is an excess of the most compact sources. Larger sources could be faint because they are genuinely distant or because they are closer but dust obscured. The effect of this selection on our redshift distribution would be a small bias towards higher-redshift objects. Nevertheless, the median K-band magnitude for the spectroscopic subset is 18.3 compared with 18.7 for the full sample (with known QSOs removed). This indicates that the spectroscopic sample is representative of the full sample, with the slightly brighter median simply due to the fact that we have had more NTT than VLT observing time. The USS-selected literature samples also have median K-band magnitudes for their spectroscopic samples that are $\leqslant 0.2$ magnitudes brighter than for the full K-band samples.

A more stringent test of whether the spectroscopic samples are typical of the complete samples is to compare flux density distributions. In Fig. 10 we compare the flux density distributions from Paper II (fig. 10) with those from the literature. The sources with redshifts from the MRCR–SUMSS, SUMSS-NVSS, 6C**, CENSORS and McCarthy samples are all consistent with being drawn randomly from the flux density distributions of the whole K-band samples, based on Kolmogorov-Smirnov test p values of 0.97, 0.986, 0.910, 0.864 and 0.58 respectively. The p value of 0.099 for the De Breuck et al. (2001, 2002) sample indicates that the sources with redshifts from this sample are somewhat less representative of the original K-band population.

Now that it is clear there are no strong biases in the K-band selection or the flux densities of the sources that have redshifts, we can investigate the corresponding redshift distributions. The CENSORS, McCarthy and 3CRR/6C*/6CE/7CRS redshift distributions in Fig. 10 are weighted towards low redshifts, while the USS-selected samples have returned higher median redshifts, as expected. The different selection frequencies and spectral indices result in the variation in flux densities between samples. In Paper II we found that the K-magnitude distribution did not vary as a function of flux density. The redshift distributions for the USS samples also do not correlate with flux density. On the one hand, the SUMSS–NVSS and MRCR–SUMSS samples have similar median redshifts but markedly different flux densities. On the other hand, the two samples netting the highest redshifts have high median flux densities.

In Paper II, we discussed how the k-correction would predict that samples selected at lower radio frequencies should result in a higher median redshift. Considering just the groups that have been shown to have redshifts representative of the full sample, the MRCR–SUMSS, SUMSS–NVSS and 6C** have selection frequencies of 408, 843 and 151 MHz respectively. For these three samples the median redshift does not correlate with selection frequency, supporting a picture in which the k-correction is not responsible for the steep spectral-energy distribution of high-redshift sources.

An alternative explanation for the steep-spectral-energy distribution of radio galaxies was given by Athreya & Kapahi (1998). They suggested that higher-density regions at high redshift reduce the hotspot velocities through the intergalactic medium, resulting in steeper electron-energy distributions. Klamer et al. (2006) then proposed that the mounting evidence that HzRGs live in over-dense regions or protoclusters (e.g. Carilli et al. 1997; Kurk et al. 2000b; Pentericci et al. 2000; Steidel et al. 2005; Kodama et al. 2007; Venemans et al. 2007) and the fact that their radio spectral energy distributions are straight, implies that the z–α correlation is due to the dense environment at high redshift. Fig. 11 shows spectral index versus redshift for MRCR–SUMSS and for three USS-selected samples and one non-USS-selected sample from the literature. All three USS-

selected literature samples have a nominal spectral index cut-off of $\alpha = -1.3$, while the MRCR–SUMSS cut-off was -1.0. The non-USS-selected sample is based on the data in McCarthy et al. (1996; 2007, private communication), from which the sources with redshifts were cross-matched with the NVSS catalogue and a spectral index was calculated between 408 and 1400 MHz. Fig. 11 shows an apparent trend in spectral index with redshift for the USS-selected sources which is not real; it arises because the spectral index cut-off in each sample has been breached by objects whose spectral index changed after sample selection because of revised flux densities. Neither the points in the literature samples with $\alpha < -1.3$, nor the points in the MRCR–SUMSS sample with $\alpha < -1.0$ show a significant correlation with redshift. In Fig. 10, the more stringent spectral index cut-off of $\alpha < -1.3$ of the SUMSS–NVSS sample did not result in a significantly higher redshift than did the $\alpha < -1.0$ selection of the MRCR–SUMSS and 6C** samples. However, Fig. 11 clearly illustrates that a spectral index cut-off of $\alpha = -1$ eliminates the bulk of the low redshift ($z < 1$) sources. Applying a steeper spectral index cut-off will miss many $z > 2$ objects. For the objects shown, ~ 54 per cent of the $z > 2$ galaxies, or ~ 49 per cent of the $z > 2.5$ galaxies, would be missed by an $\alpha = -1.3$ cut-off. However, the z–α correlation is most clearly defined by the lower envelope in the z–α plane, which is seen best in the non-USS-selected points.

If the higher-density environment at high redshift drives the steep radio spectra, then it is interesting to note that in Fig. 11, the sources steeper than $\alpha < -1.3$ are no more likely to be at high redshift than at low redshift. However, the source numbers are low, so we have also plotted the full MRCR–SUMSS K-band sample against spectral index in Fig. 12. While an individual K magnitude is not a direct indicator of redshift (see Section 4.1.2), if the net distribution of K magnitudes becomes fainter at higher redshift then the α versus K plot in Fig. 12 should show a trend for sources with $\alpha < -1.0$. However, there is no evidence that the USS sources steepen further with fainter K magnitudes, suggesting there is no advantage in selecting a more stringent spectral index cut-off.

So far, USS-selected samples have been efficient at finding high-redshift radio galaxies, although non-USS samples have also identified many $z > 2$ objects that may well have been missed by USS selection (e.g. Brookes et al. 2006, 2008). While the USS-selection nets higher-redshift samples (Fig. 10), a secondary gain is that USS-selection requires substantially less observing to return the same redshift benefits. For example, CENSORS has 122 sources in a 6 deg^2 field, while the USS-selected SUMSS–NVSS and MRCR–SUMSS samples have 65 and 162 (160 with 4-arcsec-aperture magnitudes) K-band objects respectively across the sky. Considering only the $K \geqslant 19$ galaxies which are potentially the most distant, the USS-selected samples have > 1.5 times the percentage of $K \geqslant 19$ objects than the non-USS sample. Of the $K \geqslant 19$ sources with spectroscopic redshifts, the USS-selected samples have a larger fraction of high-redshift ($z > 2.5$) objects, but the numbers are small, especially for the SUMSS–NVSS sample. This means that the non-USS sample would require at least 1.5 times more $K-$band imaging than the USS samples in order to net a smaller percentage of high redshifts. Therefore, if the aim

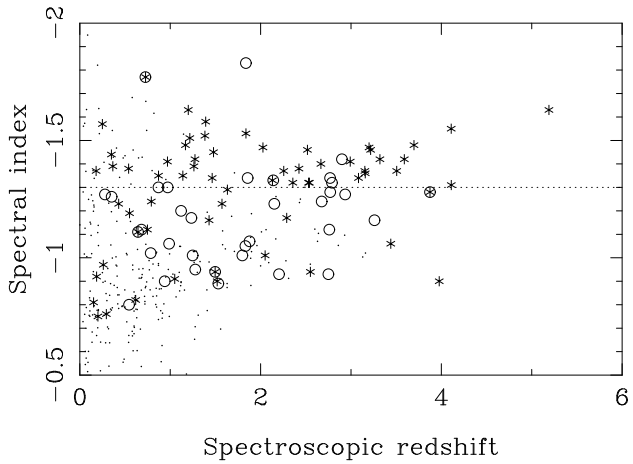

Figure 11. Spectral index versus spectroscopic redshift for our MRCR–SUMSS sample (circles; using $\alpha_{7-\rm point}$ from Paper II table 3 or, for sources without 4800- and 8640-MHz radio data, we used $\alpha_{5-\rm point}$ or α_{843}^{1400} from Paper II table 2) and three samples from the literature (stars): De Breuck et al. (2001, 2002) (using $\alpha_{\sim 350}^{1400}$), SUMSS–NVSS sample (using linear fitted spectral indices from Klamer et al. (2006), or when unavailable, α_{843}^{1400}) and Bornancini et al. (2007) (α_{325}^{1400}). The dotted line shows the spectral index cut-off of the literature samples (except a small number of sources from De Breuck et al. (2001, 2002) had a cut-off at $\alpha < -1.2$), while our MRCR–SUMSS cut-off is at $\alpha = -1.0$. In each sample there are some sources which have shallower spectral indices than the cut-offs because of subsequent revisions of source flux densities in the catalogues. The small dots are from the non-USS-selected sample of McCarthy et al. (1996; 2007, private communication), with a spectral index measured between 408 and 1400 MHz (see text for details).

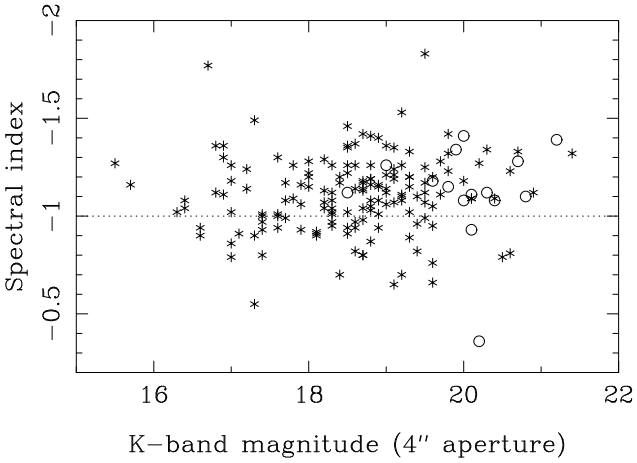

Figure 12. Spectral index versus K-band magnitude in a 4-arcsec aperture for our MRCR–SUMSS sample. The spectral indices are the 7-point fitted values from Paper II table 3 for sources that have 4800- and 8640-MHz radio data, otherwise we used the 5-point fitted values or, when unavailable, the α_{843}^{1400} values as defined in Paper II (table 2). Our spectral index cut-off was defined using 408–843 MHz, and therefore some of our sources turned out to be flatter when fitted over a large frequency range, and some had the 843-MHz flux densities revised by the new SUMSS catalogue (version 2.0), as discussed in Paper I. The sources with K-band magnitude limits are marked by a circle rather than a right-pointing arrow, for clarity. For sources steeper than -1.0, there is no correlation between spectral index and K magnitude.

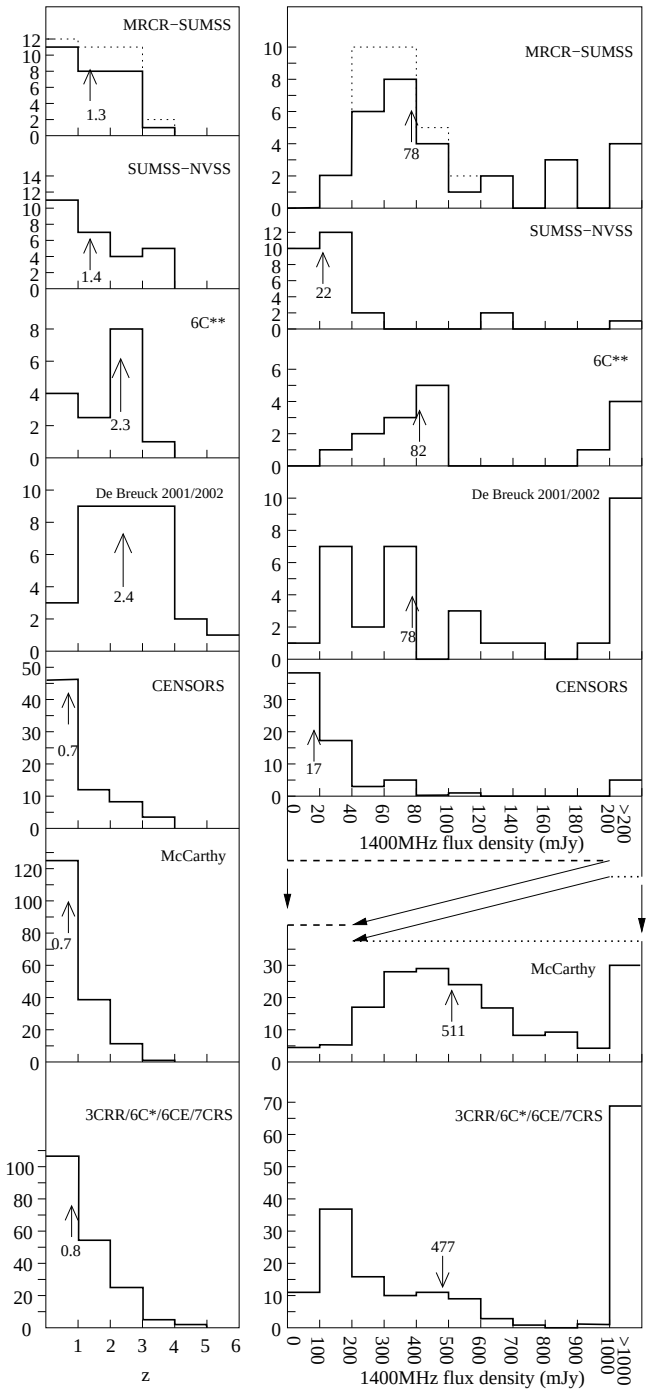

Figure 10. Distributions of redshifts and 1400 MHz flux densities for the samples from MRCR–SUMSS, SUMSS–NVSS (De Breuck et al. 2004, 2006), De Breuck et al. (2001, 2002), 6C** (Cruz et al. 2006), CENSORS (Brookes et al. 2006, 2008), McCarthy et al. (1996; 2007, private communication) and a combined sample from the 3CRR, 6C*, 6CE and 7CRS catalogues (compiled by Willott et al. 2003). Paper II included histograms of the flux densities of all the sources with K-band magnitudes, while here we show the flux densities of the subset of sources with redshifts. The CENSORS redshift histogram includes both the galaxies for which we had calculated a 4-arcsec magnitude in Paper II as well as those that only had 3-arcsec-aperture magnitudes and hence are not in the K-magnitude histogram of Paper II. Both the McCarthy and De Breuck et al. (2001, 2002) samples only have data shown if the K magnitude was measured, while sources with a redshift but no K magnitude are not included. This was done because we are comparing the redshift distributions of K-band-selected galaxies and those which did not have K magnitudes were based on different selection criteria. Vertical arrows mark the median values in each plot. QSOs have been removed from the literature samples. The redshift distribution for the MRCR–SUMSS sample shows both the radio galaxies and QSOs (dotted line) and just the radio galaxies (solid line), but the median calculation did not include the QSOs, in order to be directly comparable, to the literature samples.

is principally to get a high-redshift sample of objects, then USS selection will reduce the amount of imaging required.

4.5 Spectral line diagnostics

The bright UV emission lines in HzRGs can be produced by one of several ionisation mechanisms. The central AGN can photoionise the emission-line region gas, while shock ionisation can result from the expanding cocoon associated with the radio jets, which shocks the lower temperature gas clouds embedded within the higher temperature gas surrounding the AGN. In high-redshift galaxies, UV emission lines are shifted into the optical band, and can be used to distinguish between shock and photoionisation processes. De Breuck et al. (2000b) discuss in detail the different models for shock excitation (based on the models of Dopita & Sutherland 1996) and photoionisation (based on models by Villar-Martín, Tadhunter & Clark 1997 and Allen, Dopita & Tsvetanov 1998) resulting in a set of diagnostic line-ratio plots. In Fig. 13, we have reproduced those models on the plots of the line ratios for our galaxies. There are 13 spectra in Fig. 1 which have at least two of the UV diagnostic lines C IVλ1549, He IIλ1640 and C III]λ1909. For the sources which show only two of the three lines, we determined 3σ upper limits to the flux from the missing line. Following Hobbs (1984), the limiting flux was calculated from the product of three times the rms fluctuation in the continuum and a line width Δv. For He II we set Δv equal to the width of the C IV line (since they are both permitted lines with similar ionisation potentials), while for C III] we set Δv equal to the instrumental resolution, since this line is typically narrow in radio galaxies. All of the galaxies plotted have $z > 1.8$.

The diagnostic diagrams show that all of the galaxies are consistent with photoionisation as the primary excitation process. There are no galaxies which can be explained by shocks alone or shock plus precursor excitation, but there is one with a limiting arrow which may extend to the shock models. The majority of our galaxies lie between the lines representing photoionisation models where the incident photoionising continuum has a power law spectral index of $\alpha > -1.5$ and ionisation parameters of $-2.5 < \log_{10}(U) < -1.5$. These results agree with the much larger sample of HzRGs presented in De Breuck et al. (2000b). McCarthy (1993) produced a composite spectrum for $0.1 < z < 3$ radio galaxies, which also demonstrated the dominance of photoionisation in radio galaxies.

The QSOs in Fig. 13 typically lie above the galaxies in each plot due to a comparatively smaller He II line flux. The composite QSO spectrum from the Sloan Digital Sky Survey (Vanden Berk et al. 2001) has $\log(\mathrm{C\,III]/He\,II}) = 1.5$ and $\log(\mathrm{C\,IV/He\,II}) = 1.7$, which are very much higher than the QSOs in our sample. The QSOs in our sample have ratios much closer to that of the radio galaxies. Compact Steep-Spectrum (CSS) radio QSOs from Baker & Hunstead (1995) similarly showed stronger He II than typical QSOs.

In Paper II, we found that some sources in our sample show alignment between the radio structures and either the major axis of the fitted K-band ellipsoid, or the linear extended K-band emission. It was proposed that this alignment could be due to jet-induced star formation or alternatively, scattering of the nuclear emission along paths carved out by the jets through the gas. NVSS J210814−350823, NVSS J213637−340318 and NVSS J223101−353227 have an ellipsoid major axis aligned within 10 degrees of the radio axis (see Paper II), and are included on the emission line diagnostic plots in Fig. 13. All three have line ratios that do not match the shock models. On the one hand, we may expect shock excitation in regions of jet-induced star formation, but on the other hand, our spectra were extracted in $\sim$ 1-arcsec apertures, which will be dominated by the nuclear source. Therefore we can not rule out jet-induced star formation on the basis of the line ratios alone.

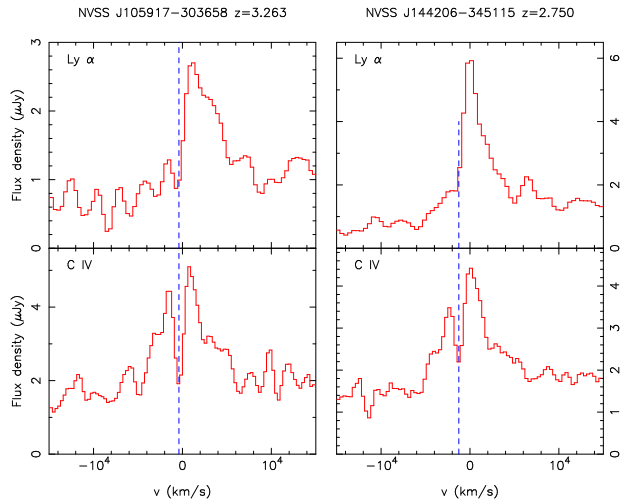

Figure 14. Line profiles of Lyα and C IVλ1549 on a common velocity scale for the two sources which show self-absorption, NVSS J105917−303658 and NVSS J144206−345115. The position of the common absorption is marked with the dashed line. The velocity origin was determined by the redshift in Table 2.

The spectra of HzRGs are typically dominated by the Lyα line in the UV spectrum. Lyα halos can extend to hundreds of kiloparsecs around the radio source (Kurk et al. 2000a; Venemans et al. 2002; Reuland et al. 2007). H I gas surrounding the active nucleus, or along the line of sight, can absorb Lyα, cutting off the blue wing of the spectral line. van Ojik et al. (1997) and De Breuck et al. (2000b, fig. 11) have shown that high-redshift galaxies with absorption in the Lyα line tend to have compact radio structures (< 50 kpc). While the resolution of our spectra is insufficient to examine the Lyα profile in detail, there are two quasars in the MRCR–SUMSS sample with obvious absorption in the blue wing of the Lyα line. The absorption profiles are shown in Fig. 14. NVSS J105917−303658 and NVSS J144206−345115 have compact linear sizes of 7.6 and 7.2 kpc, and have broad lines. The small apparent size may be due to alignment of the jets to the line-of-sight, or the jets may be intrinsically compact. In the latter case, these two sources are consistent with the findings of van Ojik et al. (1997) and De Breuck et al. (2000b) that stronger H I absorption of the Lyα line may be due to a denser medium surrounding and confining the radio source. An alternative model involves a low-density medium with an absorbing halo of low-metallicity gas which has not yet been impacted by the radio jets (Binette, Kurk, Villar-Martín, Röttgering 2000). Evidence for denser environments around these and other sources will be discussed further in a subsequent paper based on Faraday rotation measures and galaxy overdensities in the surrounding fields.

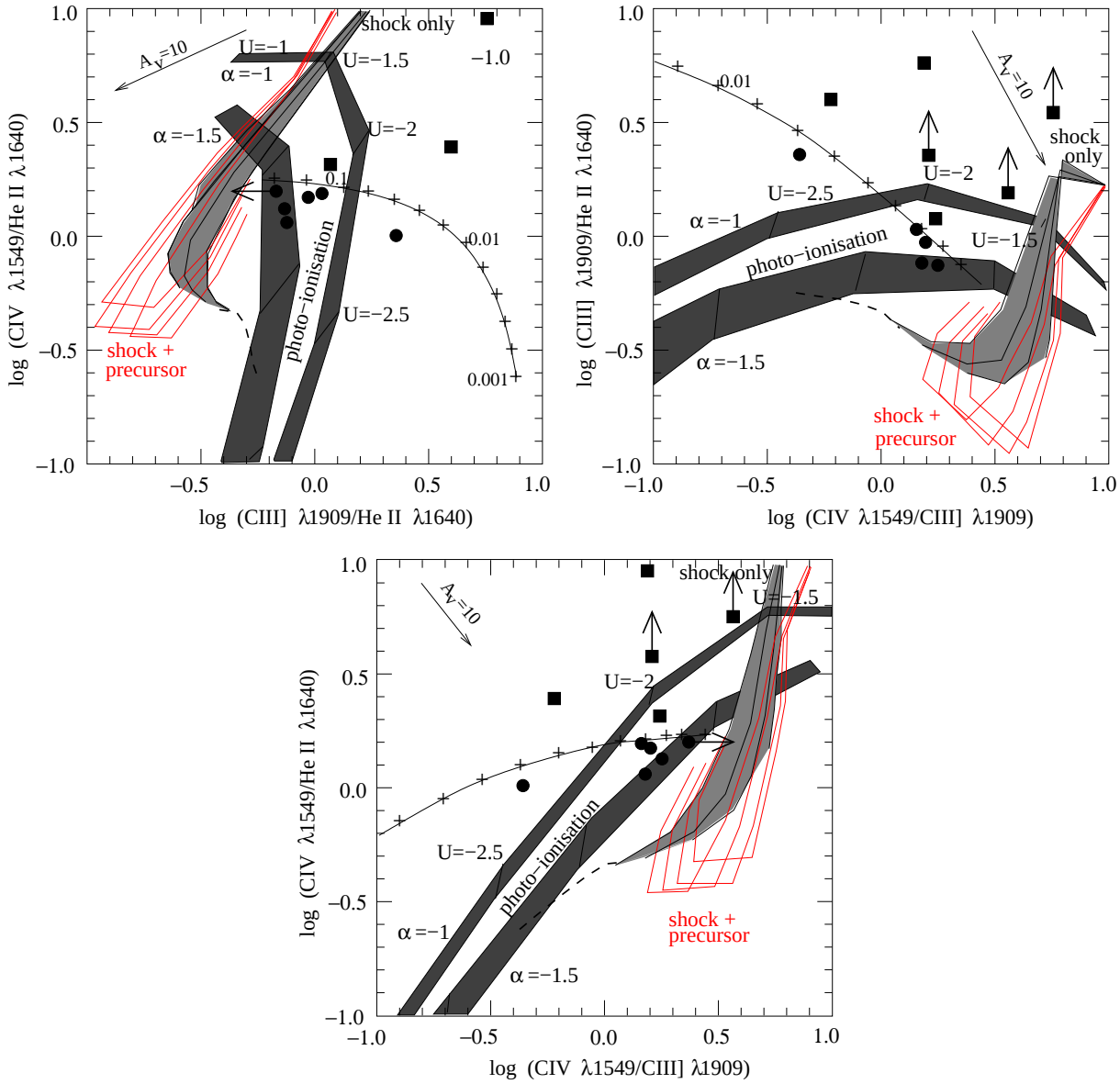

Figure 13. *UV* spectral line diagnostic plots for the lines C IVλ1549, C III]λ1909 and He IIλ1640. The galaxies in our sample that have at least two of these lines have been plotted (dots). In some cases an upper limit has been used for one of the lines. Radio galaxies are marked by dots, while the QSOs have square symbols. We have also plotted photoionisation and shock models reproduced directly from De Breuck et al. (2000b); the details of the model parameters are discussed in that paper. The light grey shaded grid represents shock models while the unshaded grid (which partially overlaps the shock models) shows the shock+precursor models. The shock velocities start at 150 km s^{-1} at the top right of the curves, and increase along the curves to 500 km s^{-1} at the end. The four curves in each grid represent four values of the magnetic parameter $0 < B/\sqrt{n} < 4\mu$G cm$^{3/2}$. Shock models for 500–1000 km s^{-1} with $n = 1.0$ and $B = 3.23$ from Allen et al. (2008) are marked by a dashed line. The dark grey shaded grids represent photoionisation models with four photo-ionisation sequences, with values of the ionisation parameter $\log_{10}(U)$ every 0.5 dex. The top and bottom shaded photoionisation grids have two models each, with power law spectral indices of $\alpha = -1$ and $\alpha = -1.5$ respectively. The left or bottom edge of the photoionisation grids are models with hydrogen density $n = 100$ cm^{-3} and the top or right edges have $n = 1000$ cm^{-3}. The single line with crosses along it represents the model of Binette, Wilson & Storchi-Bergmann (1996). This model assumes that the photoionised light has gone through both matter-bound and ionisation-bound clouds in which the ratio of the solid angle subtended by the matter-bounded to ionisation-bounded clouds is varied from 0.01 to 100 along the line with tick marks every 0.02 dex. An arrow represents 10 magnitudes of extinction based on the Milky Way extinction law from Allen, Dopita & Tsvetanov (1998). Two QSOs (NVSS J152123−375708 and NVSS J152435−352623) have upper limits on the flux of their He IIλ1640 lines which give C IV/He II> 1 and for NVSS J152435−352623 C III]/He II> 1 and therefore these values are outside the region plotted.

Dust in elliptical galaxies is typically associated with recent mergers. If HzRGs are forming through hierarchical mergers, which may be the trigger for the nuclear engine and hence the radio jets, then we might expect the most compact, newly-triggered sources to show dust extinction. We now consider the evidence for dust from spectral lines. While Lyα is generally the strongest *UV* emission line in HzRG spectra, it is not a good measure of dust as it is more likely to be be weak relative to the other *UV* lines as a result of viewing angle effects rather than dust (Villar-Martín, Binette & Fosbury 1996). Based on the dust extinction vectors calculated by Allen, Dopita & Tsvetanov (1998, fig. 4), the C III]λ1909 line is more affected by dust than C IVλ1549. Therefore, in spectra such as that for NVSS J215226−341606, the marginal detection of C III]λ1909 may be indicative of dust obscuration, although there are insufficient other lines to confirm this. The only other galaxy in which C III]λ1909 was not detected when He IIλ1640 and/or C IVλ1549 were detected is NVSS J144932−385657. In this case, based on an upper limit on the C III]λ1909 line, the diagnostic diagrams from Allen, Dopita & Tsvetanov (1998, fig. 4) can explain the lack of C III]λ1909 with either photoionisation or shock models, without the need for large dust extinction.

5 CONCLUSIONS

Spectroscopic results and analysis of the radio, K-band and redshift data have been presented for a large Southern hemisphere USS-selected HzRG survey, the MRCR–SUMSS sample. Our main findings are:

(i) Based on 175 images and 52 spectra, 164 radio sources have K-band or SuperCOSMOS identifications with 36 confirmed galaxy redshifts. The highest new redshift found is 3.26, but our spectroscopic followup is so far only 30 per cent complete. A comparison of the USS samples with the non-USS-selected CENSORS and McCarthy samples shows that the fraction of $z < 1$ galaxies is significantly reduced by USS-selection, as expected. However, for the USS-selected samples there is no correlation between the median redshift and either median flux density or selection frequency.

(ii) Detailed analysis of the K–z distribution includes a fit to 4-arcsec-aperture K magnitudes for several samples from the literature. This fit is compared with the 64-kpc fits of Willott et al. (2003) and De Breuck et al. (2004). The MRCR–SUMSS sample agrees with the Rocca-Volmerange et al. (2004) models for $> 10^{11}\mathrm{M}_{\odot}$ galaxies for all but two sources. We find no evidence for an increase in dispersion in the K–z plot at $z > 2$ and conclude that these galaxies have undergone passive stellar evolution since $z > 3$.

(iii) To test for curvature in the radio-spectral-energy distribution at frequencies lower than our selection frequency, both the MRCR–SUMSS and the SUMSS–NVSS samples were cross-matched with the 74-MHz VLSS catalogue and 151-MHz MRT catalogues. 75 per cent (15/20) of the sources with K-band magnitudes have radio-spectral-energy distributions that can be fitted by a single power-law.

(iv) The k-correction has frequently been assumed to account for the $z - \alpha$ correlation and hence for the success of USS-selection in finding high-redshift-radio galaxies. The predominance of straight spectrum objects over frequency ranges up to 74–8640 MHz and the lack of correlation with selection frequency are both evidence that an entirely different mechanism is responsible for the steep spectra of high redshift radio galaxies. Suggestions by Klamer et al. (2006) that the steep spectrum is due to the higher-density environments at high redshift will be tested for the MRCR–SUMSS sample in a subsequent paper.

(v) The spectral line ratios indicate that photoionisation is more dominant than shocks as the ionisation mechanism at the centre of these galaxies. QSOs in our sample have line ratios that are much closer to that of the radio galaxies than typical QSO ratios due to a stronger He IIλ1640 line, which is also seen in CSS sources. We find no evidence for significant dust extinction around the nucleus of any of our sources based on the line ratios.

Our method has been successful in identifying twelve $2 < z < 3.5$ galaxies which are at the epoch when the star formation rate density of the Universe was at a peak. They form an important sample for investigating the environments and evolution of massive galaxies. By the time the spectroscopic followup is complete, we expect more than 40 galaxies in this redshift range. In an upcoming paper, we will present clustering and evolution studies based on rotation measures and source overdensities in our images.

This paper has been typeset from a TEX/ LATEX file prepared by the author.

Acknowledgements

We acknowledge financial support from the *Access to Major Research Facilities Programme* which is a component of the *International Science Linkages Programme* established under the Australian Government's innovation statement, *Backing Australia's Ability*.

Australian access to the Magellan Telescopes was supported through the Major National Research Facilities program of the Australian Federal Government.

JWB acknowledges the receipt of both an Australian Postgraduate Award and a Denison Merit Award. RWH, HMJ and JJB acknowledge support from the Australian Research Council and the University of Sydney Bridging Support Grants Scheme. BMG acknowledges the support of a Federation Fellowship from the Australian Research Council through grant FF0561298.

The expertise of Scott Croom was invaluable in the QSO identifications, and we really appreciate his advice. We thank Elaine Sadler for many useful discussions, Pat McCarthy for providing his unpublished data, David Crawford for providing the MRCR, and the team at the Magellan Telescopes for their exceptional efficiency and good humour. We appreciate the assistance of the friendly staff at both the NTT and VLT. We very much thank the referees for their detailed suggestions which improved the paper.

The Australia Telescope Compact Array is part of the Australia Telescope which is funded by the Commonwealth of Australia for operation as a National Facility managed by CSIRO. SuperCOSMOS Sky Survey material is based on photographic data originating from the UK, Palomar and ESO Schmidt telescopes and is provided by the Wide-Field

Astronomy Unit, Institute for Astronomy, University of Edinburgh. This research has made use of the NASA/IPAC Extragalactic Database (NED) which is operated by the Jet Propulsion Laboratory, California Institute of Technology, under contract with the National Aeronautics and Space Administration. IRAF is distributed by the National Optical Astronomy Observatories, which are operated by the Association of Universities for Research in Astronomy, Inc., under cooperative agreement with the National Science Foundation. This publication makes use of data products from the Two Micron All Sky Survey, which is a joint project of the University of Massachusetts and the Infrared Processing and Analysis Center/California Institute of Technology, funded by the National Aeronautics and Space Administration and the National Science Foundation.

REFERENCES

Allen M. G., Dopita M. A., Tsvetanov Z. I., 1998, ApJ, 493, 571
Allen M. G., Groves B. A., Dopita M. A., Sutherland R. S., Kewley L. J., 2008, ApJS, 178, 20
Antonucci R., 1993, ARA&A, 31, 473
Appenzeller I. et al. 1998, ESO Messenger, 94, 1
Athreya R. M., Kapahi V. K., 1998, J. Astrophys. Astron., 19, 63
Baker J. C., Hunstead R. W., 1995, ApJ, 452, L95
Baker J. C., Hunstead R. W., Athreya R. M., Barthel P. D., de Silva E., Lehnert M. D., Saunders R. D. E., 2002, ApJ, 568, 592
Barthel P. D., Miley G. K., 1988, Nature, 333, 319
Barthel P. D., 1989, ApJ, 336, 606
Becker R. H., White R. L., Helfand D. J., 1995, ApJ, 450, 559
Bhatnagar S., Krishna G., Wisotzki L., 1998, MNRAS, 299, L25
Bicknell G. V., Sutherland R. S., van Breugel W. J. M., Dopita M. A., Dey A., Miley G. K., 2000, ApJ, 540, 678
Binette L., Wilson A., Storchi-Bergmann T., 1996, A&A, 312, 365
Binette L., Kurk J. D., Villar-Martín M., Röttgering H. J. A., 2000, A&A, 356, 23
Blundell K. M., Rawlings S., Eales S. A., Taylor G. B., Bradley A. D., 1998, MNRAS, 295, 265
Blundell K. M., Rawlings S., Willott C. J., 1999, AJ, 117, 677
Blundell K. M., Rawlings S., Willott C. J., Kassim N. E., Perley, R., 2002 NewAR, 46, 75.
Bock D. C-J., Large M. I., Sadler E. M., 1999, AJ 117, 1578
Bornancini C. G., De Breuck C., de Vries W., Croft S., van Breugel W., Röttgering H., Minniti D., 2007, MNRAS, 378, 551.
Bower R. G., Benson A. J., Malbon R., Helly J. C., Frenk C. S., Baugh C. M., Cole S., Lacey C. G., 2006, MNRAS, 370, 645
Broderick J. W., Bryant J. J., Hunstead R. W., Sadler E. M., Murphy T., 2007 MNRAS, 381, 341 (Paper I)
Brookes M. H., Best P. N., Rengelink R., Röttgering H. J. A., 2006, MNRAS, 366, 1265.
Brookes M. H., Best P. N., Peacock M. H., Röttgering H. J. A., Dunlop J. S., 2008, MNRAS, in press.
Bryant J. J., Broderick J. W., Johnston H. M.,Hunstead R. W., Gaensler B. M., De Breuck C., 2009, MNRAS submitted (Paper II)
Burgess A. M., Hunstead R. W., 2006, AJ, 131, 100
Carilli C. L., Röttgering H. J. A., van Ojik R., Miley G. K., van Breugel W. J. M., 1997, ApJS, 109, 1
Cohen A. S., Lane W. M., Cotton W. D., Kassim N. E., Lazio T. J. W., Perley R. A., Condon J. J., Erickson W. C., 2007, AJ, 134, 1245
Condon J. J. et al., 1998 AJ 115, 1693
Croft S. et al., 2006, ApJ, 647, 1040
Croston J. H., Hardcastle M. J., Harris D. E., Belsole E., Birkinshaw M., Worrall D. M., 2005, ApJ, 626, 733
Croton D. J. et al., 2006, MNRAS, 365, 11
Cruz M. J. et al., 2006, MNRAS, 373, 1531.
De Breuck C., van Breugel W., Röttgering H. J. A., Miley G., 2000a, A&AS, 143, 303
De Breuck C., Röttgering H. J. A., Miley G., van Breugel W., Best P., 2000b, A&A, 362, 519
De Breuck C., et al., 2001, AJ, 121, 1241
De Breuck C., van Breugel W., Stanford S. A., Röttgering H. J. A., Miley G., Stern D., 2002, AJ, 123, 637.
De Breuck C., Hunstead R. W., Sadler E. M., Rocca-Volmerange B., Klamer I., 2004, MNRAS 347, 837.
De Breuck, Klamer I., Johnston H., Hunstead R. W., Bryant J. J., Rocca-Volmerange B., Sadler E. M., 2006, MNRAS, 366, 58.
De Lucia G., Springel V., White S. D. M., Croton D., Kauffmann G., 2006, MNRAS, 366, 499
Dekker H., Delabre B., D'Odorico S., 1986, in SPIE: Instrumentation in astronomy VI; Proceedings of the Meeting, Tucson, AZ, Mar. 4-8, 1986. Part 1, 627, 39
Dopita M., Sutherland R., 1996, ApJS, 102, 161
Eales, Rawlings S., Law-green D., Cotter G., Lacy M., 1997, MNRAS, 291, 593.
El Bouchefry K., Cress C. M., 2007, AN, 328, 577
Feulner G., Gabasch A., Salvato M., Drory N., Hopp U., Bender R., 2005, ApJ, 633, L9
Fioc M., Rocca-Volmerange B., 1997, A&A, 326, 950.
Gillingham P. Jones D., 2000, in Masanori I., Moorwood A. F. M., eds., Proc. SPIE: Optical and IR Telescope Instrumentation and Detectors, 4008, 1084.
Hambly N. C. et al., 2001, MNRAS, 326, 1279.
Helfand D., Schnee S., Becker R., White R., McMahon R., 1999, AJ, 117, 1568
Hobbs L. M., 1984, ApJ, 280, 132
Hopkins A. M., 2004, ApJ, 615, 209
Hopkins A. M., Beacom J. F., 2006, ApJ, 651, 142
Jarvis M. J., Rawling S., Eales S., Blundell K. M., Bunker A. J., Croft S., McLure R. J., Willott C. J., 2001, MNRAS, 326, 1585.
Kapahi V. K., Subrahmanya C. R., Kulkarni V.K., 1987 J. Astophys. Astron., 8, 33.
Kellermann K. I., Pauliny-Toth I. I. K., Williams P. J. S., 1969, ApJ, 157, 1
Kodama T., Tanaka I., Kajisawa M., Kurk J., Venemans B., De Breuck C., Vernet J., Lidman C., 2007, MNRAS, 377, 1717
Klamer, I. J., Ekers R. D., Sadler E. M., Hunstead R.W., 2004, ApJ, 612, L97
Klamer I., Ekers R. D., Bryant J. J., Hunstead R. W., Sadler E. M., De Breuck C., 2006, MNRAS, 371, 852.

Kurk, J. D., Röttgering H. J. A., Pentericci, L., Miley, G. K., 2000a, in Mazure A., Le Févre O., Le Brun V., eds, ASP Conf. Ser.: Clustering at high redshift, 200, 424.
Kurk, J. D. et al., 2000b, A&A, 358, L1
Laing R. A., Peacock J. A., 1980, MNRAS, 190, 903
Large, M. I., Mills B. Y., Little A. G., Crawford D. F., Sutton J. M., 1981 MNRAS, 194, 693
Lehnert M. D., van Breugel W. J. M., Heckman T. M., Miley G., 1999, ApJS, 124, 11
Lilly S. J., Le Fèvre O., Hammer F., Crampton D., 1996, ApJ, 460, L1
Madau P., Ferguson H. C., Dickinson M. E., Giavalisco M., Steidel C. C., Fruchter A., 1996, MNRAS, 283, 1388
Martini P., Persson S. E., Murphy D. C., Birk C., Schectman S. A., Gunnels S. M., Koch E., 2004, in Moorwood A. F. M., Masanori I., eds, Proc SPIE: Ground-based Instrumentation for Astronomy, 5492, 1653.
Mauch T., Murphy T., Buttery H. J., Curran J., Hunstead R. W., Piestrzynski B., Robertson J. G., Sadler E., 2003 MNRAS 342, 1117
McCarthy P. J., 1993, ARA&A, 31, 639
McCarthy P. J., Kapahi V. K., van Breugel W., Persson S. E., Athreya R. M., Subrahmanya C. R., 1996, ApJS, 107, 19
Nelson A. E., Gonzalez A. H., Zaritsky D., Dalcanton J. J., 2001, ApJ, 563, 629
Owen F. N., Ledlow M. J., 1997, ApJS, 108, 41
Pandey, V., 2006, PhD thesis, Raman Research Institute, Bangalore, India.
Pentericci L., van Reeven W., Carilli C. L., Röttgering H. J. A., Miley G. K., 2000, A&AS, 145, 121
Pentericci L., Röttgering H. J. A., Miley G. K., McCarthy P., Spinrad H., van Breugel W. J. M., Macchetto F., 1999, A&AS, 341, 329
Prestage R. M., Peacock J. A., 1988, MNRAS, 230, 131
Rees, M. J., 1989, MNRAS, 239, 1P
Reuland, M. et al. 2007, AJ, 133, 2607.
Riley J. M., Warner P. J., Rawling S., Saunders R., Pooley G. G., Eales S. A., 1988, MNRAS, 236, 13p
Rocca-Volmerange B., Le Borgne D., De Breuck C., Fioc M., Moy E., 2004, A&A, 415, 931.
Rodgers A. W., Conroy P., Bloxham G., 1988, PASP, 100, 626
Röttgering H. J. A., van Ojik R., Miley G. K., Chambers K. C., van Breugel W. J. M., de Koff S., 1997, A&A, 326, 505
Seymour N. et al., 2007, ApJS 171, 353.
Silk, J., 2005, MNRAS, 364, 1337
Skrutskie M. F. et al., 2006, AJ, 131, 1163
Springel V., Di Matteo T., Hernquist L., 2005, ApJ, 620, L79
Stanford S. A., Eisenhardt P. R., Dickinson M., 1998, ApJ, 492, 461
Steidel C. C., Adelberger K. L., Shapley A. E., Erb D., Reddy N., Pettini M., 2005, ApJ, 626, 44
Thomas D., Maraston C., Bender R., Mendez de Oliveira C., 2005, ApJ, 621, 673
Urry C.M., Padovani P., 1995, PASP, 107, 803
van Breugel W. J. M., Stanford S. A., Spinrad H., Stern D., Graham J. R., 1998, ApJ, 502, 614
Vanden Berk D. E. et al., 2001, AJ, 122, 549
van Ojik R., Röttgering H. J. A., Miley G. K., Hunstead R. W., 1997, A&A, 317, 358
Venemans, B. P. et al., 2002, ApJ, 569, L11
Venemans, B. P. et al., 2007, A&A, 461, 823
Villar-Martín M., Binette L., Fosbury R. A. E., 1996, A&A, 312, 751
Villar-Martín M., Tadhunter C., Clark N., 1997, A&A, 323, 21
White R. L., Becker R. H., 1992, ApJS, 79, 331
Willott C., Rawlings S., Blundell K., Lacy M., 1999, MNRAS, 309, 1017
Willott C., Rawlings S., Jarvis M., Blundell K., 2003, MNRAS, 339, 173